



## Characterization of Iron in Lake Towuti sediment

Rachel Y. Sheppard<sup>a,\*</sup>, Ralph E. Milliken<sup>a</sup>, James M. Russell<sup>a</sup>, M. Darby Dyar<sup>b,c</sup>, Elizabeth C. Sklute<sup>b</sup>, Hendrik Vogel<sup>d</sup>, Martin Melles<sup>e</sup>, Satria Bijaksana<sup>f</sup>, Marina A. Morlock<sup>d</sup>, Ascelina K.M. Hasberg<sup>e</sup>

<sup>a</sup> Department of Earth, Environmental, and Planetary Sciences, Brown University, United States of America

<sup>b</sup> Department of Astronomy, Mt. Holyoke College, United States of America

<sup>c</sup> Planetary Science Institute, United States of America

<sup>d</sup> Institute of Geological Sciences & Oeschger Centre for Climate Change Research, University of Bern, Switzerland

<sup>e</sup> Institute of Geology and Mineralogy, University of Cologne, Germany

<sup>f</sup> Faculty of Mining and Petroleum Engineering, Institut Teknologi Bandung, Indonesia

### ARTICLE INFO

Editor: E. B Michael

#### Keywords:

Fe oxides

Sedimentation

Redox-stratified lake

Mars analogue

### ABSTRACT

Sediments collected from Lake Towuti, an ultramafic-hosted lake in Indonesia, preserve a visible alternating pattern of red and green sediments due to variations in clay mineral and Fe-oxide composition and abundance consistent with changes in iron oxidation state through time. Spectral, mineralogical, and chemical analyses on soils, river, and sediment samples from across the lake and its catchment were carried out to better understand the starting composition of these sediments and the processes that affected them before and after deposition. Despite high Fe abundances in all samples and abundant Fe oxides in lateritic source regions, mineralogical analyses (X-ray diffraction (XRD) and Mössbauer spectroscopy) of the modern lake sediment show almost no well-crystalline iron oxides. In addition, sequential Fe extractions suggest an increasing proportion of easily extractable, poorly crystalline (X-ray amorphous) material with burial depth. XRD, bulk chemistry, and visible-near infrared (VNIR) spectral reflectance measurements demonstrate that clay mineralogy and bulk chemistry can be inferred from VNIR data. These results provide evidence for variations in Fe mineralogy and crystallinity based on location in this source to sink system. Understanding how the mineralogy and chemistry of sediments within a ferruginous lake basin are affected by transport, chemical alteration, physical alteration, and deposition from source to sink on Earth, and the degree to which these trends and underlying processes can be inferred from chemical and spectral properties, may provide useful direction in assessing paleoenvironmental conditions in other terrestrial lakes as well as ancient lacustrine environments preserved in the stratigraphic record of Mars.

### 1. Introduction

The oxidation state of redox-sensitive elements in lake sediment and cores can encode information on water column conditions and potentially the relative position of the oxycline and/or shoreline. Thus, tracking oxidation state changes and mineral hosts of iron during sediment weathering, transport, deposition, and diagenesis can elucidate varying redox conditions in modern and ancient depositional environments.

Iron is of particular interest as it is ubiquitous in mafic systems found on Earth and Mars. Here we examine a suite of samples from Lake Towuti, Indonesia, to characterize the nature of Fe in the sediment of a modern terrestrial redox-stratified lake. We analyze sediment sampled from soils, rivers, and the lakebed itself in an attempt to discriminate

between processes affecting the mineral hosts of Fe during weathering in the source region, fluvial transport, and early diagenesis in the sediment column. We also examine if key mineralogical and chemical trends, including variations in clay mineralogy, Fe mineralogy and Fe oxidation state, can be inferred from Mössbauer and near-infrared reflectance spectroscopy of the bulk sediment. Understanding spatial variations in the mineralogy and chemistry of the uppermost surface sediment across the modern lakebed, and the causes of these variations, can provide a foundation for interpreting sediments in deeper lake cores. Characterizing the hosts of Fe across the modern transport and depositional system can thus aid in the reconstruction of paleoenvironmental conditions in the broader Lake Towuti region. Information on the nature and evolution of Fe-bearing phases in Lake Towuti may also provide insight into the chemical and mineralogical evolution of an

\* Corresponding author.

E-mail address: [rachel\\_sheppard@brown.edu](mailto:rachel_sheppard@brown.edu) (R.Y. Sheppard).

<https://doi.org/10.1016/j.chemgeo.2019.02.029>

Received 22 August 2018; Received in revised form 17 January 2019; Accepted 17 February 2019

Available online 01 March 2019

0009-2541/ © 2019 Elsevier B.V. All rights reserved.

ancient redox-stratified lake purported to exist on Mars (Hurowitz et al., 2017). Assessing relationships between bulk chemical and spectral properties can also lend new insight into how rapid, non-destructive techniques such as visible-near infrared reflectance spectroscopy may be used to decipher past aqueous and atmospheric conditions in fine-grained sediments and mudstones.

## 2. Background

### 2.1. Malili Lakes: Physical hydrological and geological setting

Lake Towuti is the largest lake in the Malili Lakes system, a set of five tectonic lakes located near the equator on Sulawesi island, Indonesia (2.75°S, 121.5°E, 318 m a.s.l.). It is situated in the East Sulawesi Ophiolite which is composed primarily of unserpentinized harzburgite, dunite, and serpentinized lherzolite that are a source of large quantities of iron and other metals delivered to the lake (Kadarusman et al., 2004). Lake Towuti is fed by several rivers that drain a catchment of approximately 1280 km<sup>2</sup> (Hasberg et al., 2018). The main inlet, the Mahalona River, drains two smaller upstream lakes, Matano and Mahalona, which run almost exclusively through a mix of serpentinized and unserpentinized peridotite, as well as some presently unidentified ultramafic terrain (Costa et al., 2015). The Mahalona River is also fed by the Lampenisu catchment to the northeast, and sources a large deposit of coarse-grained sediment associated with a prograding delta extending approximately 10 km into Lake Towuti (Vogel et al., 2015). Several other smaller rivers also feed into Lake Towuti, with catchments composed of serpentinized and unserpentinized peridotite and, on the east side of the lake, areas of metasediment and limestone (Costa et al., 2015). The major outlet, the Larona River, drains Lake Towuti to the west where the bedrock is unidentified ultramafic and minor sandstone/siltstone (Fig. 1, Costa et al., 2015). Because of its significant depth, ranging up to ~200 m, and tropical setting, Towuti is a thermally and redox-stratified lake (Costa et al., 2015; Vuillemin et al., 2016). The entire lake system is sulfate-poor (Crowe et al., 2008; Vuillemin et al., 2016).

### 2.2. Lake Towuti: Studies of sediment and the water column

Lake Towuti possesses a rare continuous record of tropical sedimentation spanning several glacial cycles, and the system has been used

to study sediment response to short- and long-term climate changes (Russell et al., 2014; Vogel et al., 2015; Russell et al., 2016). Sediment in the Lake Towuti catchment is sourced from a mafic/ultramafic provenance (Kadarusman et al., 2004), thus has elevated concentrations of redox sensitive elements. Consequently, the lake sediment may provide a record of redox conditions in the lake over time. Prior studies have examined changes during the past ~60 kyrs and demonstrate that trends in Fe and other redox-sensitive trace elements record more oxidizing conditions during dry periods (Costa et al., 2015). Redox cycling in the system is suggested by the presence of a down-core pattern of alternating red and green silty clays (Costa et al., 2015; Vogel et al., 2015). Consistent with this, previous work has shown that that red sediment is enriched in iron, presumed to be ferric oxides, that form when cold, dry periods induce deep mixing and oxygenation of the lake, resulting in oxidation of the bottom waters (Costa et al., 2015). This is a useful heuristic model for changes in lake sediment geochemistry through time, but to date there has been little attempt to investigate the mineralogy of iron sources and sinks in the present-day lake, nor mineralogical changes that accompany the variations in sedimentary Fe concentrations in the past.

Initial studies of modern sedimentation in the lake examined a limited number of surface sediment samples from a transect across the northern part of the lake (Weber et al., 2015) and samples from the Mahalona delta and nearby rivers (Goudge et al., 2017). Both studies concluded that the major types of clay minerals in those samples could be identified from VNIR reflectance spectra and that the strength of absorption features within the spectra were correlated with chemical composition of the bulk sample. Recent studies used a larger suite of surface sediment samples to track sedimentation across the lake, concluding that the Mahalona River is the main source of serpentine and its influence relative to kaolinite-bearing rivers can be traced in sample X-ray diffraction (XRD) patterns, mid-infrared (MIR) spectra, and elemental abundances (Morlock et al., 2018; Hasberg et al., 2018). However, these studies focused on silicate mineral sources and sinks, not iron oxides. This study presents analyses for a set of samples used in previous studies (Goudge et al., 2017; Hasberg et al., 2018; Morlock et al., 2018) that span the Lake Towuti system from source (catchment soils) to sink (lake surface sediment samples distributed across the entire basin). We examine if previously reported chemical and clay mineral trends associated with VNIR spectral features are observed within sediments from Lake Towuti as a whole. In addition to characterizing

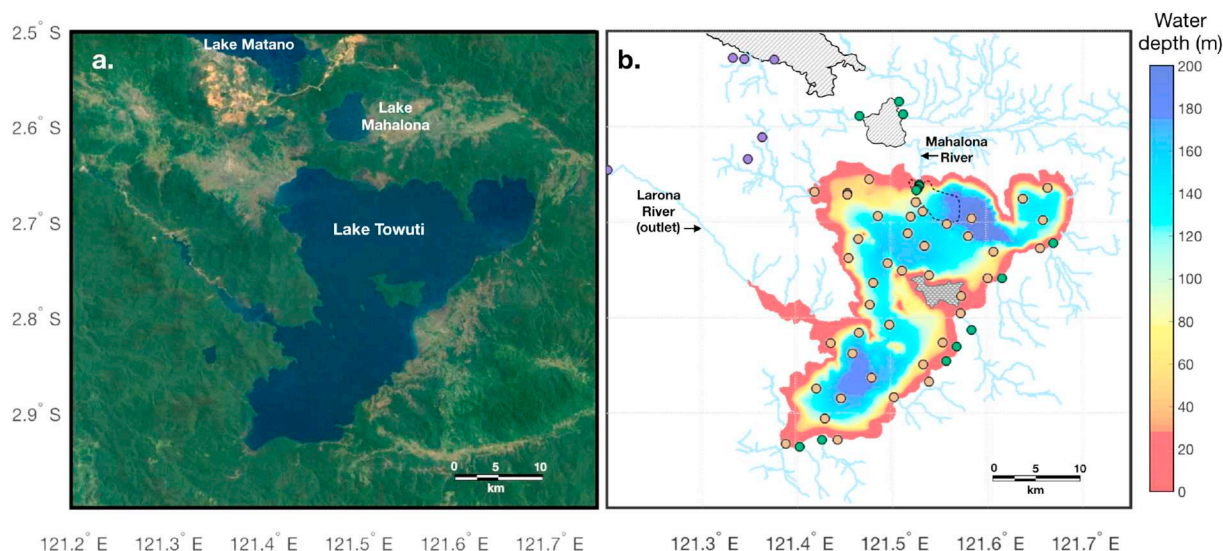


**Fig. 1.** The Malili Lakes System and associated rivers. *a.* Landsat composite image of the Malili Lakes System, including the southeastern tip of Lake Matano, Lake Mahalona, and Towuti. *b.* Bathymetry of Lake Towuti (m). Rivers are in light blue and the delta of coarse-grained material carried in by the Mahalona River is outlined by a dashed line. Brown points designate locations of surface sediment sample locations, green are river bedload samples, and purple are laterite samples. (For interpretation of the references to colour in this figure legend, the reader is referred to the web version of this article.)

**Table 1**  
Sample location information, grain size (from Hasberg et al., 2018), and analyses performed. (– indicates not measured or not applicable. VNIR sp. = VNIR reflectance spectroscopy, Ex. 1 and Ex. 2 are sequential extractions described in Table 2, Mossb. = Mössbauer spectroscopy, XRD = X-ray diffraction, ICP = ICP-AES for elemental abundances.)

Sample No.	Type	Latitude	Longitude	Water depth (m)	Depth in laterite bed (m)	Depth in core (m)	% sand	% silt	% clay	Analyses performed
133	River	–2.573333	121.509050	0.28	–	–	–	–	–	VNIR sp, XRD
134	River	–2.573333	121.509050	0.28	–	–	–	–	–	VNIR sp, XRD
135	River	–2.758320	121.617050	0.70	–	–	–	–	–	VNIR sp, XRD
136	River	–2.927380	121.428300	0.40	–	–	–	–	–	VNIR sp, XRD
137	River	–2.660290	121.529940	1.00	–	–	–	–	–	VNIR sp, XRD
138	River	–2.662050	121.530200	0.50	–	–	–	–	–	VNIR sp, XRD
139	River	–2.665210	121.528220	1.50	–	–	–	–	–	VNIR sp, XRD
140	River	–2.666140	121.527440	2.50	–	–	–	–	–	VNIR sp, XRD
141	River	–2.721880	121.670770	0.80	–	–	–	–	–	VNIR sp, XRD
142	River	–2.721880	121.670770	1.40	–	–	–	–	–	VNIR sp, XRD
143	River	–2.845450	121.558220	0.50	–	–	–	–	–	VNIR sp, XRD
144	River	–2.588817	121.467333	–	–	–	–	–	–	VNIR sp, XRD
145	River	–2.587000	121.513300	0.50	–	–	–	–	–	VNIR sp, XRD
146	River	–2.830231	121.569557	–	–	–	–	–	–	VNIR sp, XRD
147	River	–2.935080	121.405030	0.70	–	–	–	–	–	VNIR sp, XRD
148	River	–2.812530	121.585230	1.00	–	–	–	–	–	VNIR sp, XRD
226	Laterite (bed 1)	–2.528883	121.346800	0.00	0.40	–	–	–	–	VNIR sp, XRD, ICP
227	Laterite (bed 1)	–2.528883	121.346800	0.00	1.00	–	–	–	–	VNIR sp, XRD, ICP
228	Laterite (bed 1)	–2.528883	121.346800	0.00	1.50	–	–	–	–	VNIR sp, XRD, ICP
229	Laterite (bed 1)	–2.528883	121.346800	0.00	2.20	–	–	–	–	VNIR sp, XRD, ICP
230	Laterite (bed 2)	–2.528100	121.334867	0.00	0.10	–	–	–	–	VNIR sp, XRD, ICP
506	Laterite sample 230 after Extraction 1	–	–	–	–	–	–	–	–	Ex. 1, VNIR sp, XRD
518	Laterite sample 230 after Extraction 2	–	–	–	–	–	–	–	–	Ex. 1 & 2, VNIR sp, XRD
231	Laterite (bed 2)	–2.528100	121.334867	0.00	2.00	–	–	–	–	VNIR sp, XRD, ICP
507	Laterite sample 231 after Extraction 1	–	–	–	–	–	–	–	–	Ex. 1, VNIR sp
519	Laterite sample 231 after Extraction 2	–	–	–	–	–	–	–	–	Ex. 1 & 2, VNIR sp
232	Laterite (bed 3)	–2.644950	121.203617	0.00	0.30	–	–	–	–	VNIR sp, XRD, ICP
233	Laterite (bed 3)	–2.644950	121.203617	0.00	1.00	–	–	–	–	VNIR sp, XRD, ICP
234	Laterite (bed 4)	–2.653533	121.350733	0.00	0.40	–	–	–	–	VNIR sp, XRD, ICP
235	Laterite (bed 4)	–2.643533	121.350733	0.00	1.20	–	–	–	–	VNIR sp, XRD, ICP
508	Laterite sample 235 after Extraction 1	–	–	–	–	–	–	–	–	Ex. 1, VNIR sp
520	Laterite sample 235 after Extraction 2	–	–	–	–	–	–	–	–	Ex. 1 & 2, VNIR sp
236	Laterite (bed 4)	–2.643533	121.350733	0.00	0.05	–	–	–	–	VNIR sp, XRD, ICP
237	Laterite (bed 5)	–2.611200	121.365600	0.00	0.20	–	–	–	–	VNIR sp, XRD, ICP
238	Laterite (bed 5)	–2.611200	121.365600	0.00	1.50	–	–	–	–	VNIR sp, XRD, ICP, Mossb.
509	Laterite sample 238 after Extraction 1	–	–	–	–	–	–	–	–	Ex. 1, VNIR sp, XRD
521	Laterite sample 238 after Extraction 2	–	–	–	–	–	–	–	–	Ex. 1 & 2, VNIR sp, XRD
239	Laterite (bed 5)	–2.611200	121.365600	0.00	2.5	–	–	–	–	VNIR sp, XRD, ICP
240	Laterite (bed 6)	–2.529517	121.378400	0.00	0.10	–	–	–	–	VNIR sp, XRD, ICP
241	Laterite (bed 6)	–2.529517	121.378400	0.00	1.00	–	–	–	–	VNIR sp, XRD, ICP
242	Laterite (bed 6)	–2.529517	121.378400	0.00	1.50	–	–	–	–	VNIR sp, XRD, ICP
243	Laterite (bed 6)	–2.529517	121.378400	0.00	2.50	–	–	–	–	VNIR sp, XRD, ICP
244	Laterite (bed 6)	–2.529517	121.378400	0.00	3.50	–	–	–	–	VNIR sp, XRD, ICP
245	Laterite (bed 6)	–2.529517	121.378400	0.00	3.00	–	–	–	–	VNIR sp, XRD, ICP
247	Surface	–2.668183	121.420633	1.99	–	–	0.034	0.795	0.170	VNIR sp, XRD, ICP
248	Surface	–2.669217	121.454833	72.54	–	–	0.001	0.715	0.284	VNIR sp, XRD, ICP
249	Surface	–2.654700	121.477517	41.80	–	–	0.060	0.690	0.250	VNIR sp, XRD, ICP
250	Surface	–2.671183	121.454833	80.37	–	–	0.008	0.732	0.261	VNIR sp, XRD, ICP, Mossb.
251	Surface	–2.678817	121.526600	129.01	–	–	0.050	0.787	0.163	VNIR sp, XRD, ICP
252	Surface	–2.694317	121.520983	175.81	–	–	0.016	0.752	0.232	VNIR sp, XRD, ICP
253	Surface	–2.688333	121.533500	179.13	–	–	0.014	0.779	0.207	VNIR sp, XRD, ICP
254	Surface	–2.695733	121.585100	271.82	–	–	0.007	0.689	0.304	VNIR sp, XRD, ICP
255	Surface	–2.693483	121.486783	173.87	–	–	0.000	0.692	0.308	VNIR sp, XRD, ICP

(continued on next page)

Table 1 (continued)

Sample No.	Type	Latitude	Longitude	Water depth (m)	Depth in laterite bed (m)	Depth in core (m)	% sand	% silt	% clay	Analyses performed
256	Surface	-2.701850	121.559167	236.27	-	-	0.003	0.729	0.268	VNIR sp., XRD, ICP
510	Surface sample 256 after Extraction 1	-	-	-	-	-	-	-	-	Ex. 1, VNIR sp.
522	Surface sample 256 after Extraction 2	-	-	-	-	-	-	-	-	Ex. 1 & 2, VNIR sp.
257	Surface	-2.675250	121.638417	184.54	-	-	0.000	0.585	0.415	VNIR sp., XRD, ICP
258	Surface	-2.697633	121.659883	182.22	-	-	0.014	0.662	0.324	VNIR sp., XRD, ICP
259	Surface	-2.727433	121.656883	1.01	-	-	0.545	0.361	0.094	VNIR sp., XRD, ICP
511	Surface sample 259 after Extraction 1	-	-	-	-	-	-	-	-	Ex. 1, VNIR sp., XRD
523	Surface sample 259 after Extraction 2	-	-	-	-	-	-	-	-	Ex. 1 & 2, VNIR sp., XRD
260	Surface	-2.714633	121.581683	240.47	-	-	0.000	0.674	0.326	VNIR sp., XRD, ICP
261	Surface	-2.711333	121.518033	207.21	-	-	0.007	0.761	0.232	VNIR sp., XRD, ICP
262	Surface	-2.717317	121.466550	142.94	-	-	0.000	0.639	0.361	VNIR sp., XRD, ICP
263	Surface	-2.724583	121.535833	213.48	-	-	0.015	0.730	0.255	VNIR sp., XRD, ICP
264	Surface	-2.737617	121.456067	113.75	-	-	0.000	0.647	0.353	VNIR sp., XRD, ICP
265	Surface	-2.663617	121.664683	95.07	-	-	0.004	0.658	0.338	VNIR sp., XRD, ICP
266	Surface	-2.742833	121.497067	182.03	-	-	0.000	0.643	0.357	VNIR sp., XRD, ICP, Mossb.
267	Surface	-2.730683	121.607867	118.22	-	-	0.001	0.670	0.330	VNIR sp., XRD, ICP
268	Surface	-2.758267	121.601700	35.60	-	-	0.605	0.355	0.039	VNIR sp., XRD, ICP
269	Surface	-2.795283	121.573617	1.42	-	-	0.333	0.554	0.113	VNIR sp., XRD, ICP
270	Surface	-2.777133	121.573917	3.84	-	-	0.726	0.239	0.035	VNIR sp., XRD, ICP, Mossb.
512	Surface sample 270 after Extraction 1	-	-	-	-	-	-	-	-	Ex. 1, VNIR sp.
524	Surface sample 270 after Extraction 2	-	-	-	-	-	-	-	-	Ex. 1 & 2, VNIR sp., Mossb.
271	Surface	-2.755533	121.540467	137.23	-	-	0.001	0.681	0.318	VNIR sp., XRD, ICP
272	Surface	-2.750450	121.512283	190.65	-	-	0.000	0.681	0.319	VNIR sp., XRD, ICP
273	Surface	-2.763400	121.481800	183.57	-	-	0.000	0.644	0.356	VNIR sp., XRD, ICP
274	Surface	-2.786183	121.478083	153.82	-	-	0.000	0.621	0.379	VNIR sp., XRD, ICP
275	Surface	-2.815450	121.466950	187.85	-	-	0.000	0.572	0.428	VNIR sp., XRD, ICP
276	Surface	-2.826200	121.437283	35.98	-	-	0.000	0.553	0.447	VNIR sp., XRD, ICP
277	Surface	-2.874033	121.422017	171.33	-	-	0.000	0.586	0.414	VNIR sp., XRD, ICP
513	Surface sample 277 after Extraction 1	-	-	-	-	-	-	-	-	Ex. 1, VNIR sp., XRD
525	Surface sample 277 after Extraction 2	-	-	-	-	-	-	-	-	Ex. 1 & 2, VNIR sp., XRD
278	Surface	-2.932000	121.390400	0.54	-	-	0.421	0.462	0.116	VNIR sp., XRD, ICP
279	Surface	-2.905200	121.431267	161.28	-	-	0.029	0.621	0.351	VNIR sp., XRD, ICP
280	Surface	-2.884450	121.448050	235.65	-	-	0.000	0.601	0.399	VNIR sp., XRD, ICP
281	Surface	-2.862533	121.479833	241.34	-	-	0.000	0.642	0.358	VNIR sp., XRD, ICP
282	Surface	-2.807383	121.498967	184.13	-	-	0.000	0.657	0.343	VNIR sp., XRD, ICP
283	Surface	-2.883300	121.503900	15.78	-	-	0.103	0.706	0.191	VNIR sp., XRD, ICP
514	Surface sample 283 after Extraction 1	-	-	-	-	-	-	-	-	Ex. 1, VNIR sp.
526	Surface sample 283 after Extraction 2	-	-	-	-	-	-	-	-	Ex. 1 & 2, VNIR sp.
284	Surface	-2.848783	121.534367	67.92	-	-	0.011	0.757	0.232	VNIR sp., XRD, ICP
285	Surface	-2.825667	121.554883	63.61	-	-	0.073	0.827	0.100	VNIR sp., XRD, ICP
286	Surface	-2.837217	121.459983	234.13	-	-	0.000	0.580	0.420	VNIR sp., XRD, ICP, Mossb.
515	Surface sample 286 after Extraction 1	-	-	-	-	-	-	-	-	Ex. 1, VNIR sp., XRD
527	Surface sample 286 after Extraction 2	-	-	-	-	-	-	-	-	Ex. 1 & 2, VNIR sp., XRD, Mossb.
287	Surface	-2.927383	121.444717	1.37	-	-	0.782	0.199	0.019	VNIR sp., XRD, ICP
516	Surface sample 287 after Extraction 1	-	-	-	-	-	-	-	-	Ex. 1, VNIR sp.
528	Surface sample 287 after Extraction 2	-	-	-	-	-	-	-	-	Ex. 1 & 2, VNIR sp.
288	Surface	-2.867050	121.540550	1.01	-	-	0.591	0.343	0.066	VNIR sp., XRD, ICP
97	Core	-2.717480	121.514980	-	-	2.36	-	-	-	VNIR sp., XRD, Mossb.
489	Core sample 97 after Extraction 1	-	-	-	-	-	-	-	-	Ex. 1, VNIR sp., ICP
497	Core sample 97 after Extraction 2	-	-	-	-	-	-	-	-	Ex. 1 & 2, VNIR sp., XRD, ICP
99	Core	-2.717480	121.514980	-	-	7.72	-	-	-	VNIR sp., XRD, Mossb.
490	Core sample 99 after Extraction 1	-	-	-	-	-	-	-	-	Ex. 1, VNIR sp., ICP
498	Core sample 99 after Extraction 2	-	-	-	-	-	-	-	-	Ex. 1 & 2, VNIR sp., XRD, ICP
104	Core	-2.717480	121.514980	-	-	14.78	-	-	-	VNIR sp., XRD
491	Core sample 104 after Extraction 1	-	-	-	-	-	-	-	-	Ex. 1, VNIR sp., ICP

(continued on next page)

Table 1 (continued)

Sample No.	Type	Latitude	Longitude	Water depth (m)	Depth in laterite bed (m)	Depth in core (m)	% sand	% silt	% clay	Analyses performed
499	Core sample 104 after Extraction 2	-	-	-	-	-	-	-	-	Ex. 1 & 2, VNIR sp., XRD, ICP
113	Core	-2.717480	121.514980	-	-	26.52	-	-	-	VNIR sp., XRD
492	Core sample 113 after Extraction 1	-	-	-	-	-	-	-	-	Ex. 1, VNIR sp., ICP
500	Core sample 113 after Extraction 2	-	-	-	-	-	-	-	-	Ex. 1 & 2, VNIR sp., XRD, ICP
114	Core	-2.717480	121.514980	-	-	27.12	-	-	-	VNIR sp., XRD
493	Core sample 114 after Extraction 1	-	-	-	-	-	-	-	-	Ex. 1, VNIR sp., ICP
501	Core sample 114 after Extraction 2	-	-	-	-	-	-	-	-	Ex. 1 & 2, VNIR sp., XRD, ICP
116	Core	-2.717480	121.514980	-	-	30.16	-	-	-	VNIR sp., XRD
494	Core sample 116 after Extraction 1	-	-	-	-	-	-	-	-	Ex. 1, VNIR sp., ICP
502	Core sample 116 after Extraction 2	-	-	-	-	-	-	-	-	Ex. 1 & 2, VNIR sp., XRD, ICP
118	Core	-2.717480	121.514980	-	-	32.63	-	-	-	VNIR sp., XRD
495	Core sample 118 after Extraction 1	-	-	-	-	-	-	-	-	Ex. 1, VNIR sp., ICP
503	Core sample 118 after Extraction 2	-	-	-	-	-	-	-	-	Ex. 1 & 2, VNIR sp., XRD, ICP
121	Core	-2.717480	121.514980	-	-	75.84	-	-	-	VNIR sp., XRD
96	Core sample 121 after Extraction 1	-	-	-	-	-	-	-	-	Ex. 1, VNIR sp., ICP
504	Core sample 121 after Extraction 2	-	-	-	-	-	-	-	-	Ex. 1 & 2, VNIR sp., XRD, ICP
122	Core	-2.717480	121.514980	-	-	76.59	-	-	-	VNIR sp., XRD
505	Core sample 122 after Extraction 1	-	-	-	-	-	-	-	-	Ex. 1, VNIR sp., ICP
517	Core sample 122 after Extraction 2	-	-	-	-	-	-	-	-	Ex. 1 & 2, VNIR sp., XRD, ICP

clay mineralogy, we also evaluate differences in the mineral host(s) of Fe between these samples and determine the extent to which VNIR spectra are sensitive to changes in Fe-mineralogy, bulk mineralogy, and bulk chemistry.

### 3. Methods

#### 3.1. Sampling

Samples were collected in 2013 (Costa et al., 2015; Goudge et al., 2017) and during the 2015 Towuti Drilling Project (Russell et al., 2016), and they consist of three different sample types: lateritic soils from the catchment, inflowing river bed sediment, and surficial sediment from the lake floor (Fig. 1, Table 1).

*Lateritic soils* were collected from six separate, exposed weathered soil profiles. Because of limitations in accessibility, all sampling sites were west or northwest of the lake. The 20 soil samples were collected at different depths within the soil profiles, spanning the top of the soil bed to bedrock. Some samples were coarse-grained with distinct pebbles and many had visible pieces of organic material (Morlock et al., 2018).

*River bedload* samples were collected from twelve separate rivers. The 16 total samples were primarily collected near the river mouths, with four samples collected along the largest inlet, the Mahalona River (Weber et al., 2015; Goudge et al., 2017).

*Lake surface sediment* samples were collected from the sediment/water interface using a polnar grab sampler (UWITEC Corp., Austria). The 42 samples analyzed for this study were mostly fine-grained (most dominated by silt and clay-size material) and relatively homogeneous in appearance (Hasberg et al., 2018; Morlock et al., 2018).

*Lake sediment core* samples were collected in 2015 by the International Continental Scientific Drilling Program Towuti Drilling Project (ICDP-TDP) from Lake Towuti (Russell et al., 2016). These cores were subsampled at the LacCore facility at the University of Minnesota in 2016.

#### 3.2. Reflectance spectroscopy

The mineralogy of each sample was determined by reflectance spectroscopy (VNIR-IR wavelengths) and powder X-ray diffraction. Samples were relatively fine-grained (spanning sand to clay; for full details on grain size see Goudge et al., 2017) and so were lightly powdered using a corundum mortar and pestle. Reflectance spectra were acquired for dried, powdered samples over a wavelength range of 0.35–4.75  $\mu\text{m}$  using a combination of spectrometers in the NASA Reflectance Experiment Laboratory (RELAB) facility housed at Brown University. An Analytical Spectral Devices (ASD) FieldSpec3 spectroradiometer was used for the visible-near infrared (VIS-NIR, 0.35–2.5  $\mu\text{m}$ ) range and a Thermo Nexus 870 FTIR spectrometer was used for the near-infrared to mid-infrared (NIR-MIR, 0.8–4.75  $\mu\text{m}$ ) range. ASD reflectance spectra were acquired relative to a white Spectralon standard, whereas FTIR reflectance data were acquired relative to diffuse gold (both standards from Labsphere). The two sets of spectral data were spliced together at 1.7  $\mu\text{m}$  to provide a continuous spectrum.

VNIR spectral parameters, including band depth, were calculated for absorptions characteristic of certain minerals common to the Malili Lakes system (Fig. 2). Band depth is a measurement of the strength of an absorption feature and was calculated based on the method of Clark and Roush (1984). A variety of factors can influence the strength of an absorption band in reflectance spectra, including particle size and strong spectral contrast between absorbing species (e.g., VNIR-transparent minerals such as quartz mixed with highly absorbing, opaque minerals such as ilmenite or magnetite). All samples studied here were ground to roughly equivalent particle size and lack significant abundances of opaque phases (weak or absent peaks for magnetite and



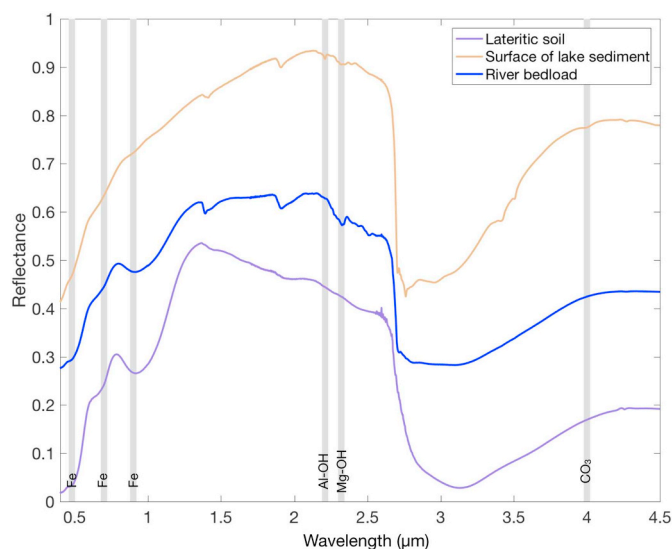


**Fig. 2.** A representative spectrum from each sample type (soil, river, and surface sediment), offset for clarity. Important absorptions are highlighted at 0.48, 0.7, and 0.9  $\mu\text{m}$  (Fe) 2.21  $\mu\text{m}$  (Al-OH), 2.32  $\mu\text{m}$  (Mg-OH), and 4.0  $\mu\text{m}$  (carbonate).

ilmenite in XRD data), thus band depth values (absorption strength) may provide a reasonable proxy for relative mineral abundance. Major mineral phases considered in the analysis of spectral data are discussed below and were based on previous studies (Goudge et al., 2017; Weber et al., 2015), XRD patterns, and qualitative analysis of the spectra themselves.

### 3.2.1. Mg serpentine

Trioctahedral Mg phyllosilicates in the serpentine group (e.g. antigorite, chrysotile, lizardite) were identified based on a prominent asymmetric absorption centered at  $\sim 2.32 \mu\text{m}$  caused by vibrations (combination bend and stretch) of the Mg–OH bond (Weber et al., 2015).

### 3.2.2. Al clays

Absorptions near  $\sim 2.2 \mu\text{m}$  are caused by combination stretch and bend of OH and metal-OH (Weber et al., 2015). The precise location of the band at 2.21  $\mu\text{m}$  and the asymmetric shoulder near 2.16  $\mu\text{m}$  seen in many sample spectra from previous studies of Lake Towuti sediment are most consistent with Al-OH vibrations in kaolinite, whereas other Al-bearing phyllosilicates (e.g. montmorillonite, illite, muscovite) exhibit a broader, more symmetric absorption in this region (Clark et al., 1990; Bishop et al., 2008; Weber et al., 2015; Goudge et al., 2017).

### 3.2.3. Fe smectite

Spectra of the dioctahedral ferric smectite nontronite exhibit a characteristic absorption at 2.28  $\mu\text{m}$  caused by vibration of the Fe–OH bond (Clark et al., 1990; Bishop et al., 2008; Weber et al., 2015). Nontronite was not specifically analyzed in previous studies of more limited sample sets, but all spectra in this study were examined for the possible presence of this mineral.

### 3.2.4. Other Fe absorptions

The presence of  $\text{Fe}^{2+/3+}$  in octahedral and tetrahedral coordination can give rise to a wide range of complex and sometimes overlapping absorptions in the 0.35–2.5  $\mu\text{m}$  wavelength range (Burns, 1993). These features are due to electronic absorptions (e.g. intervalence charge transfer, oxygen-metal charge transfer, and crystal field splitting). Features associated with  $\text{Fe}^{2+/3+}$  in oxides and poorly crystalline materials of interest to this study include absorptions at 0.48, 0.7, and 0.9  $\mu\text{m}$  (see Fig. 2). Spectra for the subset of samples processed for

sequential iron extraction (described below) were also acquired for the dried samples after each extraction step. This allows for an assessment of changes in absorptions due to relative changes in  $\text{Fe}^{2+/3+}$  during the extraction, which helps to link observed spectral absorptions to the presence of X-ray amorphous versus crystalline Fe phases.

### 3.2.5. Carbonate

A broad  $\text{CO}_3$  absorption ( $\nu_1 + \nu_3$  vibration mode) is located at 3.8–4.0  $\mu\text{m}$  (Gaffey et al., 1993; Sutter et al., 2007). This band is stronger than overtone absorptions observed at shorter wavelengths ( $< 2.5 \mu\text{m}$ ), does not overlap with OH absorptions associated with clay minerals, and is not as affected by  $\text{H}_2\text{O}$  or  $\text{CO}_2$  absorptions (Wagner and Schade, 1996).

### 3.3. X-ray diffraction

Powder X-ray diffraction (XRD) measurements were made for all samples to provide qualitative information on phase identification, including measurements of d-spacing for clay minerals. Dried, powdered samples were analyzed on a Bruker D2 Phaser XRD with a Cu K $\alpha$  source. Sample cups were filled without packing to reduce preferential orientation. XRD patterns were analyzed for presence/absence of relevant peaks, in part using the patterns of synthesized nanophase iron (oxyhydr)oxides discussed in Sklute et al. (2018) and reference patterns from data in the American Mineralogist Crystal Structure Database (AMCSD) using the CrystalDiffract software by CrystalMaker database (Fig. 3). Measurements were taken from 5 to 90  $^\circ 2\theta$  at 0.02029  $^\circ$  step size.

### 3.4. ICP-AES

Major and minor elemental abundances were determined by inductively coupled plasma-atomic emission spectrometry (ICP-AES) at Brown University. Major (Al, Ca, Cr, Fe, K, Mg, Mn, Na, Ni, P, Si, Ti) and trace (Co, Cr, Cu, Mo, Ni, Sc, Sr, V, Zn, Zr) elements were analyzed in the 42 surface samples after they were dissolved using flux fusion (Murray et al., 2000). To do so, each sample ( $0.04 \pm 0.005 \text{ g}$ ) was gently mixed with lithium metaborate flux ( $0.16 \pm 0.005 \text{ g}$ ) in a graphite crucible and fused at 1050  $^\circ\text{C}$  for 10 min. Each fused bead was then dropped into 20 mL of 10% nitric acid ( $\text{HNO}_3$ ), shaken for 30–60 min, filtered with a 0.45  $\mu\text{m}$  Gelman filter, and 5 mL of the final fused solution diluted in 35 mL of 10%  $\text{HNO}_3$ . The same process was done for standard reference materials (RGM-1, NIST1646a, BIR-1, BHVO-2, NIST2711, BCR-2, and DTS-2B).

Once diluted, the samples were analyzed on a Jobin Yvon JY2000 ICP-AES. Concentration data are calibrated to the fluxed standard reference materials run with each batch. A drift solution comprising a small amount of each diluted sample was analyzed every 12 measurements to monitor and correct for any change in signal. The detector did not saturate during these measurements.

### 3.5. Sequential iron extraction

To determine the relative amounts of highly reactive iron (e.g. amorphous Fe phases, ferrihydrite, lepidocrocite) and crystalline iron oxy/hydroxides (e.g. hematite, goethite) in the samples, a two-stage sequential iron extraction was carried out on several laterite and surface sediment samples using a protocol modified from Poulton and Canfield (2005), described in Table 2. Fe in silicates was not removed by these extractions.

The hydroxylamine HCl extraction was created by mixing 69.49 g Hy-HCl into 1 L of a 25% acetic acid solution. The extraction was performed in 50 mL plastic falcon tubes, where 100 mg of sediment and 10 mL hydroxylamine HCl were mixed and placed on a shaker table and reacted for 48 h at room temperature.

The sodium dithionite extraction was prepared by mixing 50 g of sodium dithionite and 51.6 g sodium citrate in 1 L DI water. Acetic acid

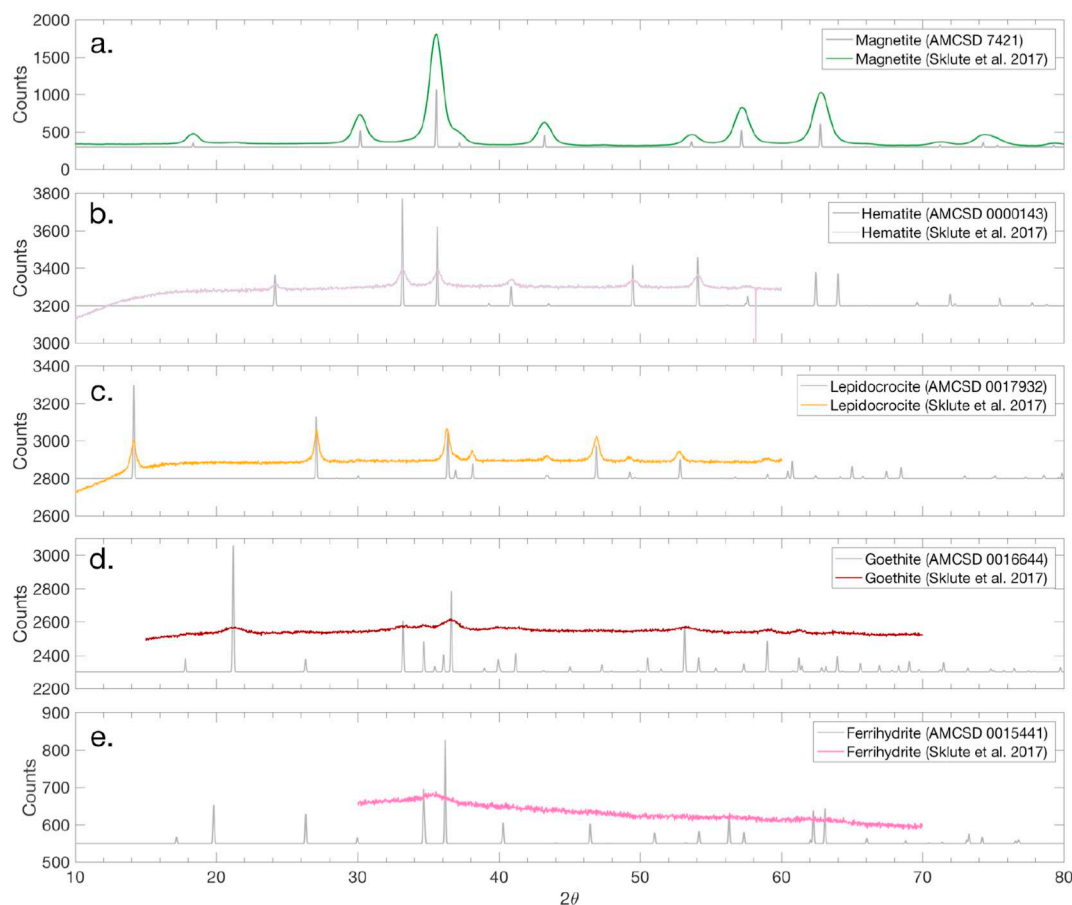


**Fig. 3.** XRD patterns of iron oxides synthesized in Sklute et al. (2018) (colored lines), with AMCSD reference patterns in gray: a. magnetite, b. hematite, c. lepidocrocite, d. goethite, and e. ferrihydrite.

**Table 2**  
Sequential Fe extraction protocol.

Extraction	Target phases	Duration
Hydroxylamine HCl	Amorphous iron oxides (e.g. ferrihydrite)	48 h
Sodium dithionite	Crystalline iron oxides (goethite and hematite)	2 h

was then added until the pH reached 4.8. Samples residues from the hydroxylamine HCl extraction were reacted with 10 mL of the sodium dithionite in falcon tubes on a shaker table for 2 h at room temperature.

After each extraction, the falcon tubes were centrifuged and supernatant poured into a vial. The residual sediment was then washed with deionized water three times, centrifuged each time, and poured into the same vial. The residual sediment was freeze dried and spectra and XRD patterns were collected to assess whether the extractions were truly removing the relevant Fe oxides. The supernatant was dried at 60 °C, rehydrated in 10 mL 2% nitric acid, diluted 1:100 in 2% nitric acid, and measured for total iron concentration on the ICP-AES.

### 3.6. Mössbauer spectroscopy

Mössbauer spectroscopy is sensitive to small energetic changes around Fe atoms and can be used to characterize coordination environments of Fe oxides in complex, heterogeneous samples (Sklute et al. in review). Mössbauer measurements were acquired at Mt. Holyoke College with the sample at 4 K, 130 K, and 295 K on a Web Research Co. (now See Co.) W100 spectrometer using a ~75–65 mCi <sup>57</sup>Co source in rhodium. Low temperature spectra were obtained using a Janis Research Co. Model 850 4 K closed-cycle helium compression

system. The spectra were fit using the Mex\_disd program and the fits were then used to derive several Mössbauer parameters (Dyar et al., 2006; Sklute et al. in review). These include center shift (CS), which reflects the s-electronic charge density, and is affected by bond characteristics, valence state, and coordination environment. This shift is presented in Mössbauer spectra as a velocity (mm/s) shift relative to α-Fe foil. Another relevant parameter is quadrupole splitting (QS) of nuclear energy levels, which creates the distinctive doublets seen in Mössbauer spectra. Changes in Fe valence state or changes to the crystal lattice that affect the coordination or bonding environment will affect this splitting and the observed doublets and sextets. Finally, the hyperfine field (hff), which results from the interaction of the nuclear magnetic moment with the net magnetic field at the nucleus, creates the distinct sextet pattern seen in Mössbauer spectrum. While the hff is sensitive to changes in the bonding environment and the crystal lattice, it is also sensitive to crystallinity and grain size. For example, grain size and composition affect the temperature at which the transition from doublet to sextet occurs, which allows ferric and ferrous Fe in different coordination environments to be distinguished by collecting spectra at multiple temperatures (4 K, 130 K, and 295 K here).

## 4. Results

### 4.1. Correlation of spectral characteristics with chemical data

The elemental abundances of all samples can be found in Table 3. Surface sediment samples show strong spatial variations in Al and Mg (Fig. 4a,b) with associated changes in silicate mineralogy, consistent with the results of previous studies. Values for Al are relatively low in the north near the Mahalona River delta and increase away from the

**Table 3**  
Chemistry results (wt%) from ICP-AES. (– indicates not measured.)

Sample no.	Type	Al <sub>2</sub> O <sub>3</sub>	FeO	MgO	SiO <sub>2</sub>	TiO <sub>2</sub>
133	River	–	–	–	–	–
134	River	–	–	–	–	–
135	River	–	–	–	–	–
136	River	–	–	–	–	–
137	River	–	–	–	–	–
138	River	–	–	–	–	–
139	River	–	–	–	–	–
140	River	–	–	–	–	–
141	River	–	–	–	–	–
142	River	–	–	–	–	–
143	River	–	–	–	–	–
144	River	–	–	–	–	–
145	River	–	–	–	–	–
146	River	–	–	–	–	–
147	River	–	–	–	–	–
148	River	–	–	–	–	–
226	Laterite (bed 1)	3.600	38.400	7.090	–	0.061
227	Laterite (bed 1)	3.280	38.100	1.050	–	0.047
228	Laterite (bed 1)	5.240	46.400	0.860	–	0.095
229	Laterite (bed 1)	2.600	24.300	1.340	–	0.029
230	Laterite (bed 2)	3.410	47.300	0.740	–	0.137
506	Laterite sample 230 after Extraction 1	–	–	–	–	–
518	Laterite sample 230 after Extraction 2	–	–	–	–	–
231	Laterite (bed 2)	2.930	48.600	1.130	–	0.108
507	Laterite sample 231 after Extraction 1	–	–	–	–	–
519	Laterite sample 231 after Extraction 2	–	–	–	–	–
232	Laterite (bed 3)	2.870	12.300	12.800	–	0.106
233	Laterite (bed 3)	2.170	14.900	10.800	–	0.047
234	Laterite (bed 4)	4.360	33.900	4.750	–	0.148
235	Laterite (bed 4)	4.840	18.300	4.130	–	0.170
508	Laterite sample 235 after Extraction 1	–	–	–	–	–
520	Laterite sample 235 after Extraction 2	–	–	–	–	–
236	Laterite (bed 4)	5.910	14.900	7.300	–	0.220
237	Laterite (bed 5)	5.250	49.100	0.610	–	0.111
238	Laterite (bed 5)	4.200	49.400	0.610	–	0.062
509	Laterite sample 238 after Extraction 1	–	–	–	–	–
521	Laterite sample 238 after Extraction 2	–	–	–	–	–
239	Laterite (bed 5)	3.730	49.100	0.620	–	0.059
240	Laterite (bed 6)	4.580	34.900	2.080	–	0.067
241	Laterite (bed 6)	8.250	33.800	3.220	–	0.068
242	Laterite (bed 6)	8.290	32.900	3.380	–	0.077
243	Laterite (bed 6)	2.170	40.900	2.250	–	0.043
244	Laterite (bed 6)	3.260	21.800	8.260	–	0.082
245	Laterite (bed 6)	2.000	14.300	9.310	–	0.050
247	Surface	12.429	12.458	5.976	49.106	0.882
248	Surface	13.229	15.138	5.731	42.950	0.922
249	Surface	9.423	20.636	7.641	39.266	0.480
250	Surface	8.666	13.083	11.918	38.961	0.431
251	Surface	6.180	11.687	18.219	41.885	0.255
252	Surface	7.782	14.102	13.216	39.235	0.334
253	Surface	7.257	12.184	14.688	39.143	0.307
254	Surface	8.470	17.191	9.882	37.126	0.323
255	Surface	10.483	15.998	7.774	38.222	0.515
256	Surface	8.483	15.360	11.400	37.006	0.333
510	Surface sample 256 after Extraction 1	–	–	–	–	–
522	Surface sample 256 after Extraction 2	–	–	–	–	–
257	Surface	8.058	23.128	6.378	30.811	0.259
258	Surface	6.635	23.003	6.967	29.796	0.207
259	Surface	5.698	25.302	5.749	28.869	0.126
511	Surface sample 259 after Extraction 1	–	–	–	–	–
523	Surface sample 259 after Extraction 2	–	–	–	–	–
260	Surface	8.510	16.311	9.066	35.024	0.353
261	Surface	7.969	13.427	12.775	38.703	0.324
262	Surface	10.906	16.371	7.558	39.555	0.494
263	Surface	8.419	15.271	11.242	38.404	0.330
264	Surface	10.121	17.291	6.794	37.649	0.439
265	Surface	7.198	23.427	5.618	31.635	0.226
266	Surface	9.931	15.659	8.863	39.460	0.427
267	Surface	9.044	19.058	7.076	35.082	0.373
268	Surface	5.280	21.700	13.554	33.676	0.168
269	Surface	9.541	12.580	4.374	52.465	0.576
270	Surface	6.118	27.767	5.134	35.524	0.168
512	Surface sample 270 after Extraction 1	–	–	–	–	–
524	Surface sample 270 after Extraction 2	–	–	–	–	–

(continued on next page)



Table 3 (continued)

Sample no.	Type	Al <sub>2</sub> O <sub>3</sub>	FeO	MgO	SiO <sub>2</sub>	TiO <sub>2</sub>
271	Surface	8.262	16.582	7.618	33.699	0.335
272	Surface	8.969	15.428	8.748	36.008	0.365
273	Surface	9.656	16.290	6.933	35.348	0.387
274	Surface	9.209	15.486	5.249	32.634	0.354
275	Surface	8.523	22.386	4.074	32.930	0.294
276	Surface	8.688	23.757	3.835	30.356	0.277
277	Surface	9.532	23.344	4.625	31.792	0.293
513	Surface sample 277 after Extraction 1	–	–	–	–	–
525	Surface sample 277 after Extraction 2	–	–	–	–	–
278	Surface	6.501	29.400	4.922	23.804	0.093
279	Surface	10.145	18.993	4.293	34.179	0.390
280	Surface	5.246	30.272	6.168	27.696	0.074
281	Surface	11.879	17.809	4.537	37.579	0.456
282	Surface	11.129	13.502	4.300	40.793	0.498
283	Surface	9.133	17.855	4.566	33.168	0.364
514	Surface sample 283 after Extraction 1	–	–	–	–	–
526	Surface sample 283 after Extraction 2	–	–	–	–	–
284	Surface	13.594	14.020	4.422	42.879	0.589
285	Surface	13.339	12.371	3.821	46.219	0.669
286	Surface	4.726	20.371	16.331	33.981	0.038
515	Surface sample 286 after Extraction 1	–	–	–	–	–
527	Surface sample 286 after Extraction 2	–	–	–	–	–
287	Surface	5.250	27.322	11.414	33.082	0.052
516	Surface sample 287 after Extraction 1	–	–	–	–	–
528	Surface sample 287 after Extraction 2	–	–	–	–	–
288	Surface	11.125	20.991	4.545	31.899	0.321
97	Core	–	–	–	–	–
489	Core sample 97 after Extraction 1	–	4.989	–	–	–
497	Core sample 97 after Extraction 2	–	2.177	–	–	–
99	Core	–	–	–	–	–
490	Core sample 99 after Extraction 1	–	6.930	–	–	–
498	Core sample 99 after Extraction 2	–	4.353	–	–	–
104	Core	–	–	–	–	–
491	Core sample 104 after Extraction 1	–	5.383	–	–	–
499	Core sample 104 after Extraction 2	–	4.789	–	–	–
113	Core	–	–	–	–	–
492	Core sample 113 after Extraction 1	–	6.550	–	–	–
500	Core sample 113 after Extraction 2	–	2.754	–	–	–
114	Core	–	–	–	–	–
493	Core sample 114 after Extraction 1	–	5.655	–	–	–
501	Core sample 114 after Extraction 2	–	2.962	–	–	–
116	Core	–	–	–	–	–
494	Core sample 116 after Extraction 1	–	6.461	–	–	–
502	Core sample 116 after Extraction 2	–	4.212	–	–	–
118	Core	–	–	–	–	–
495	Core sample 118 after Extraction 1	–	3.947	–	–	–
503	Core sample 118 after Extraction 2	–	2.778	–	–	–
121	Core	–	–	–	–	–
496	Core sample 121 after Extraction 1	–	8.043	–	–	–
504	Core sample 121 after Extraction 2	–	7.093	–	–	–
122	Core	–	–	–	–	–
505	Core sample 122 after Extraction 1	–	13.852	–	–	–
517	Core sample 122 after Extraction 2	–	2.672	–	–	–

river mouth and delta with movement toward more distal parts of the lake. Values for Mg exhibit the opposite trend: Mg abundance is elevated in the Mahalona River delta and drops quickly with distance from the delta.

Band depth values of the 2.21  $\mu\text{m}$  Al-OH (kaolinite) absorption in spectra of surface samples are correlated with Al<sub>2</sub>O<sub>3</sub> abundance (positive coefficient significant at  $p < 0.01$ ); for laterites the correlation is not significant (Fig. 4c). Spectra for laterite and surface samples exhibit positive correlations between band depths of the 2.32  $\mu\text{m}$  Mg-OH (serpentine) absorption and MgO abundance (positive coefficient significant at  $p < 0.01$ ; see Table 4 for additional information on regression statistics) (Fig. 4d).

Fe abundances are reported as %FeO (total Fe, not indicating redox state) and are very high in the lateritic catchment soils (Fig. 5a.), with concentrations of up to 49.4 wt%, and Fe abundances are more spatially variable between the lake sediment samples (Fig. 5b.). VNIR spectra

indicate the presence of Fe-oxides and Fe-bearing silicates in both soils and lake sediment, where the latter may include nontronite in two lake samples and several laterite samples. Because of the complex and overlapping nature of spectral absorptions of Fe at VNIR wavelengths, (Fig. 6), two different spectral parameters are compared with ICP-determined Fe abundances (Fig. 5). The inverse slope of the 0.45  $\mu\text{m}$  to 0.48  $\mu\text{m}$  absorption band, which is observed in some Fe-oxides such as hematite and goethite and is similar to a measure of band area, is correlated with Fe abundance for both laterites and surface samples (positive coefficient significant at  $p < 0.01$ ) (Fig. 5c). The band depth of the  $\sim 0.9\text{--}1.0 \mu\text{m}$  absorption that is commonly observed in Fe-oxides and Fe-bearing silicates (e.g. nontronite) is also correlated with Fe abundance (positive coefficient significant at  $p < 0.05$  for surface samples, positive coefficient significant at  $p < 0.01$  for laterites) (Fig. 5d). Although both spectral parameters exhibit a correlation with ICP-derived Fe content, the correlation is strongest for the spectral slope

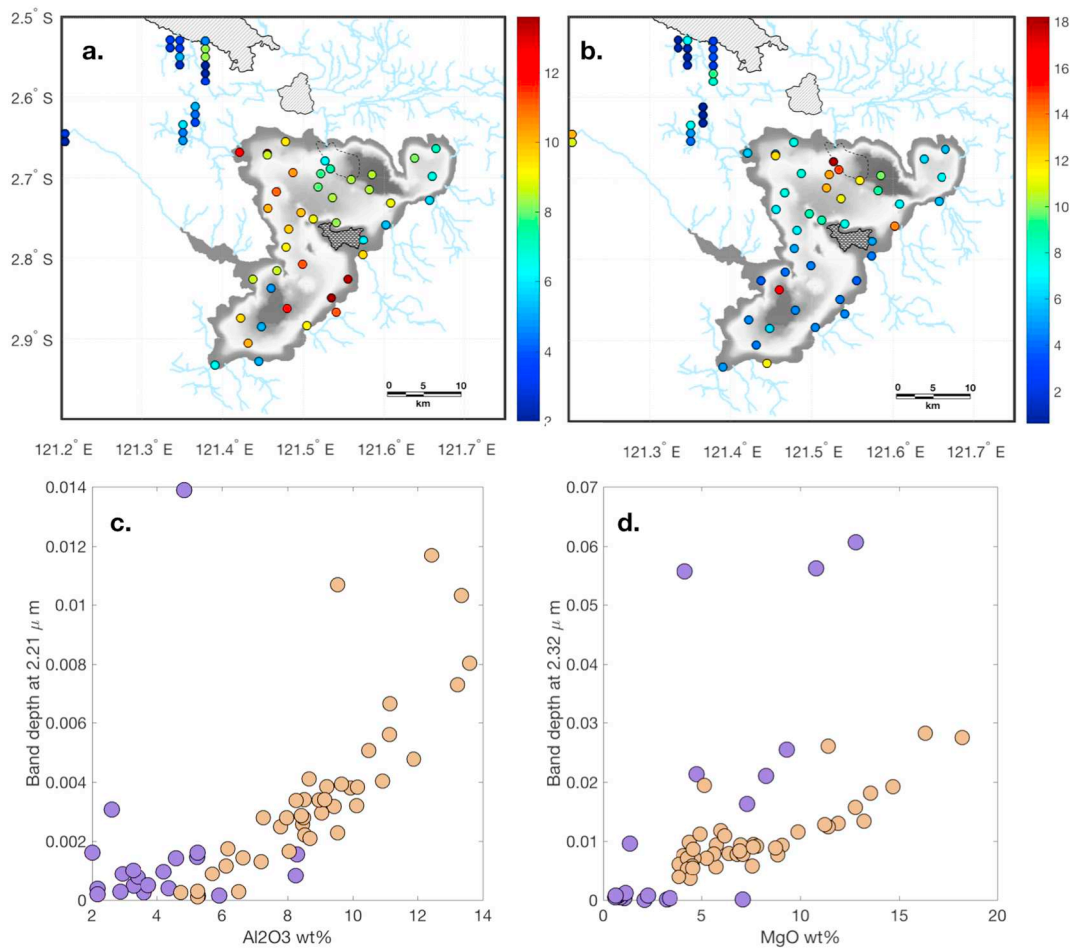


**Fig. 4.** a.  $\text{Al}_2\text{O}_3$  (wt%) in surface and soil samples. b.  $\text{MgO}$  (wt%) in surface and soil samples. c. Band depth at  $2.21\ \mu\text{m}$  versus  $\text{Al}_2\text{O}_3$  abundance in surface (brown) and soil (purple) samples. d. Band depth at  $2.32\ \mu\text{m}$  versus  $\text{MgO}$  abundance in surface (brown) and soil (purple) samples. (For interpretation of the references to colour in this figure legend, the reader is referred to the web version of this article.)

**Table 4**  
Al and Mg regression results.

	Dependent variable			
	BD $2.21\ \mu\text{m}$ , surface	BD $2.21\ \mu\text{m}$ , laterite	BD $2.32\ \mu\text{m}$ , surface	BD $2.32\ \mu\text{m}$ , laterite
	(1)	(2)	(3)	(4)
$\text{Al}_2\text{O}_3$ , surface	0.001*** (0.0001)			
$\text{Al}_2\text{O}_3$ , laterite		0.0002 (0.0004)		
$\text{MgO}$ , surface			0.001*** (0.0002)	
$\text{MgO}$ , laterite				0.004*** (0.001)
Constant	−0.005*** (0.001)	0.001 (0.002)	0.001 (0.001)	−0.003 (0.005)
Observations	42	20	42	20
$R^2$	0.700	0.012	0.644	0.580
Residual Std. error	0.002 (df = 40)	0.003 (df = 18)	0.004 (df = 40)	0.014 (df = 18)
F statistic	93.113*** (df = 1; 40)	0.210 (df = 1; 18)	72.365*** (df = 1; 40)	24.901*** (df = 1; 18)

Note: \* $p < 0.1$ ; \*\* $p < 0.05$ ; \*\*\* $p < 0.01$ .

parameter in the lake surface samples (brown points in Fig. 5c.). The correlation between this Fe spectral slope parameter is much stronger than previously reported correlations of Fe abundance with spectral properties (Weber et al., 2015). Additional information on regression

statistics is presented in Table 5.

The lateritic soil samples are characterized by high FeO abundances (25–50 wt%) that are generally highest at the top of the soil bed and decrease with depth (Morlock et al., 2018). One laterite, located west of

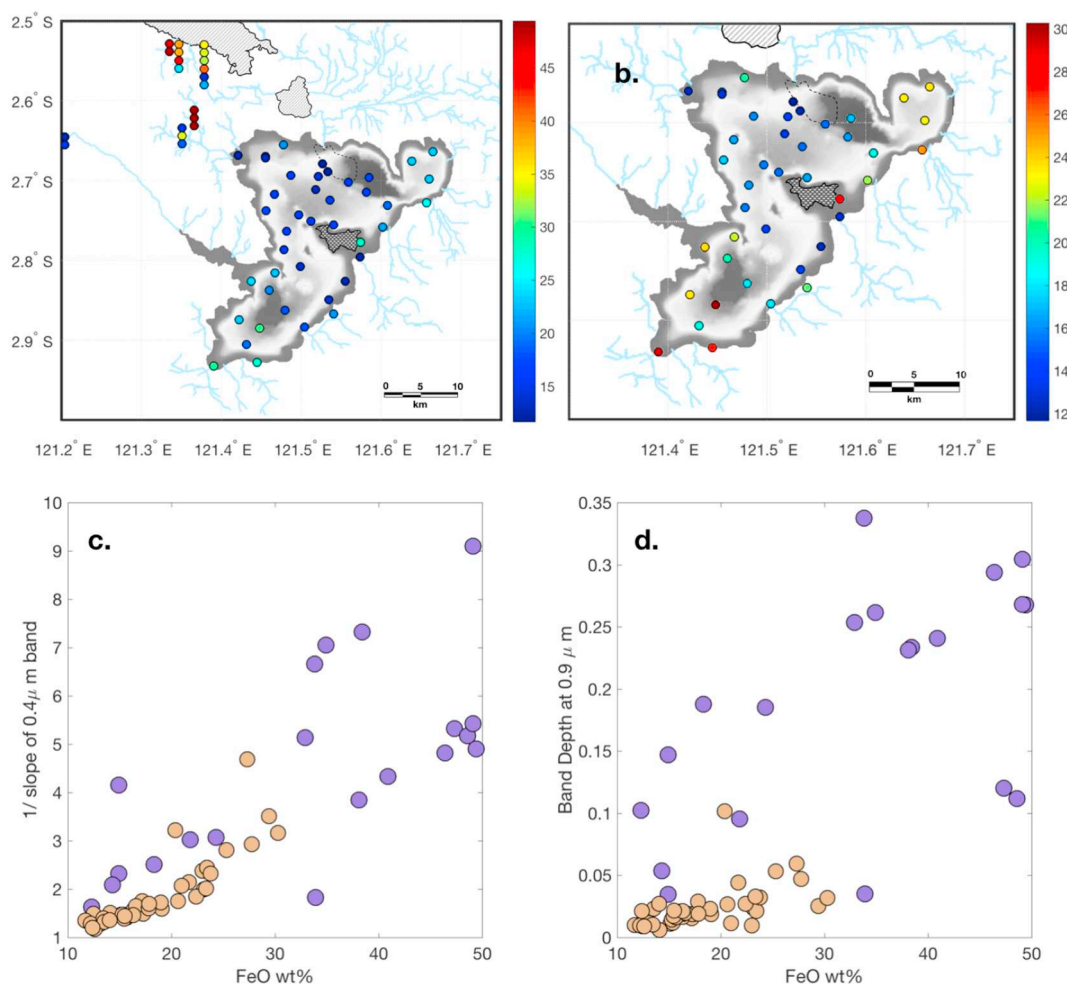


**Fig. 5.** a. ICP-determined elemental abundance of FeO (wt%) in surface and soil samples. b. ICP-determined elemental abundance of FeO (wt%) in just surface samples. c. Flatness of the 0.4 μm band versus with FeO abundance in surface sediment (brown) and soil (purple) samples. d. Band depth at 0.9 μm band versus with FeO abundance in surface (brown) and soil (purple) samples. (For interpretation of the references to colour in this figure legend, the reader is referred to the web version of this article.)

the others near the Larona River, the main outlet of Lake Towuti, has significantly lower FeO (~14 wt%; Fig. 8) and elevated MgO. All soil samples examined here have moderate-to-low  $\text{Al}_2\text{O}_3$  values (2–8 wt%) that, like FeO, tend to be highest in the samples closest to the surface. VNIR spectra from these high-Fe samples are consistent with abundant hematite and goethite, with much lower concentrations of other Fe-bearing phases such as Fe-clay minerals or siderite.

Nontronite was identified in two shallow, coastal lake surface samples (Samples 259, 270) and potentially six laterite samples based on a diagnostic (Fe-OH) absorption feature at 2.28 μm in their reflectance spectra (Fig. 7). In addition, spectra for a number of the laterite samples exhibit two distinct absorptions near ~2.28 μm and ~2.31 μm (purple spectrum, Fig. 7a). The strength of these two features varies independently within the sample group as a whole, suggesting this apparent ‘doublet’ absorption is the result of two distinct mineral phases that vary in their relative abundance between samples (i.e., the doublet is not the result of a single mineral phase). The position of the 2.28 μm feature is similar to that of Fe-OH in nontronite, and the position of the 2.31 μm feature is similar to that of Mg-OH in saponite; neither is consistent with absorptions typical of serpentine. However, the absorptions in these laterite samples are narrower than what is commonly observed in reflectance spectra of pure nontronite or saponite, thus the origin of these spectral features is somewhat ambiguous. It is possible that the observed doublet is a result of a mixture

of nontronite and saponite, perhaps poorly crystalline forms of these clay minerals.

## 4.2. Iron mineralogy

### 4.2.1. XRD patterns

Consistent with the ICP data (Fig. 5) and VNIR spectra (Figs. 6, 7), XRD patterns indicate that crystalline Fe-oxides are more abundant in laterite patterns than in lake surface sediment samples (Fig. 8). These analyses are qualitative and based on relative peak intensity. Detailed examination of the laterite XRD patterns (Fig. 9a–c) show sharp, relatively high goethite peaks in almost every laterite sample, sharp magnetite peaks in several samples, and hematite in few samples. In the surface sediment samples (Fig. 9d–f.), the peaks are broadened and shorter. There is still evidence of Fe oxides (goethite, magnetite, hematite) in the lake surface samples, but, similar to ICP results, they are less abundant compared to other iron phases such as serpentine, siderite, Cr spinel, olivine, amphibole, and pyroxene. There is also a notable paucity of well-crystalline Fe-oxides in lake sediment samples from the coarse-grained Mahalona delta deposits as well as samples located close to other river inlets (Fig. 9g.). Note that truly amorphous Fe will not appear as an amorphous “hump” as amorphous silica does, but rather raise the baseline of the XRD pattern, making it difficult to understand qualitatively or quantitatively through XRD alone.

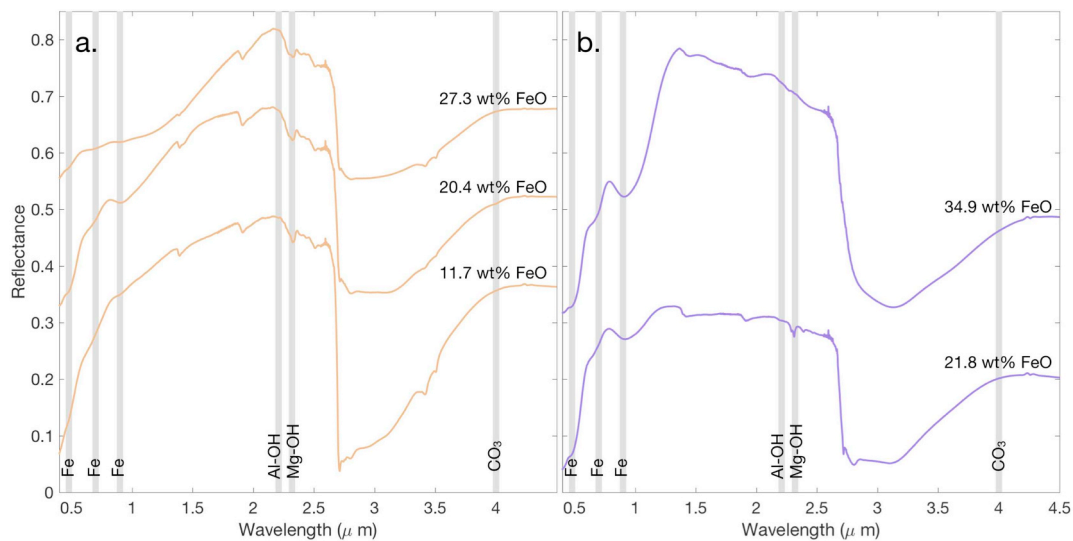


**Fig. 6.** Example spectra, with relevant band locations highlighted, labeled with their ICP-determined FeO abundances (wt%). *a.* Three example surface sediment spectra, offset for clarity. The top two are from the southern end of the lake and the bottom spectrum is from the coarse-grained, serpentine-rich Mahalona river delta. *b.* Two example laterite spectra, offset for clarity. Top spectrum is from the top of one laterite bed (10 cm from the surface) and bottom spectrum is from the bottom of the same bed (3.5 m from surface). Note the increase in Fe absorption band strengths (0.4–1.5  $\mu\text{m}$ ) and decrease in Mg-serpentine band strength ( $\sim 2.32 \mu\text{m}$ ) in the spectrum for the upper soil sample compared with that of the lower soil sample, consistent with increased abundance of Fe oxides at the expense of serpentine during progressive weathering of the serpentinized bedrock.

#### 4.2.2. Sequential Fe extraction

Sequential Fe extractions affecting the mineral hosts of iron were performed on laterites, surface samples, and samples from sediment cores (Fig. 10). The laterites, which are a dominant sediment source in this system, all exhibit significantly higher total Fe concentrations and are dominated by crystalline Fe-oxides (e.g., goethite, hematite) relative to lake sediment. Total Fe abundances are similar in the lake surface and core samples, but the manner in which this Fe is partitioned between mineral phases is quite different between the two sample groups. The proportion of Fe in amorphous or highly reactive phases (i.e. the extraction 1 supernatant) versus crystalline phases (i.e. extraction 2 supernatant) is roughly equivalent in surface sediment samples. In contrast, samples from deeper within the sediment column (core samples) contain more iron in what appear to be X-ray amorphous phases.

We note that not all of the iron is necessarily extracted by these dissolution steps, and the summed supernatant Fe abundance of some samples is up to 9 wt% Fe below that of the original surface sediment.

This “excess iron” can be partially attributed to the presence of Fe in silicates and other mineral phases that our sequential reaction protocol does not, and is not intended to, digest. However, XRD analyses of sediments prior to and after the extractions suggest that some reactive iron mineral phases survive the extraction process. For instance, the intensity of the goethite peak is reduced but a portion appears to be resistant to the extractions (Fig. 11). The intensity of the goethite peak is reduced but some goethite remains. Processing the sample with extraction 2 a second time removed additional goethite, resulting in near-complete removal of goethite peaks in the XRD patterns.

#### 4.2.3. Mössbauer spectra

Overall, Mössbauer data are in agreement with the observations of reflectance spectra, XRD patterns, and sequential extractions and further indicate that the Fe mineralogy is extremely complex within the surface sediment. The samples contain a large nanocrystalline component, both ferrous and ferric phases, and exhibit interparticle effects causing broadening of the doublets and sextets during magnetic

**Table 5**  
Fe regression results.

	Dependent variable			
	1/slope 0.4 $\mu\text{m}$ band, surface	1/slope 0.4 $\mu\text{m}$ band, laterite	BD 0.9 $\mu\text{m}$ , surface	BD 0.9 $\mu\text{m}$ , laterite
	(1)	(2)	(3)	(4)
FeO, surface	0.126*** (0.012)		0.005** (0.002)	
FeO, laterite		0.102*** (0.026)		0.008*** (0.002)
Constant	−0.437* (0.229)	1.107 (0.940)	0.118*** (0.034)	0.349*** (0.066)
Observations	42	20	42	20
R <sup>2</sup>	0.733	0.453	0.142	0.501
Residual Std. error	0.384 (df = 40)	1.536 (df = 18)	0.058 (df = 40)	0.108 (df = 18)
F Statistic	109.810*** (df = 1; 40)	14.889*** (df = 1; 18)	6.626** (df = 1; 40)	18.067*** (df = 1; 18)

Note: \* $p < 0.1$ ; \*\* $p < 0.05$ ; \*\*\* $p < 0.01$ .

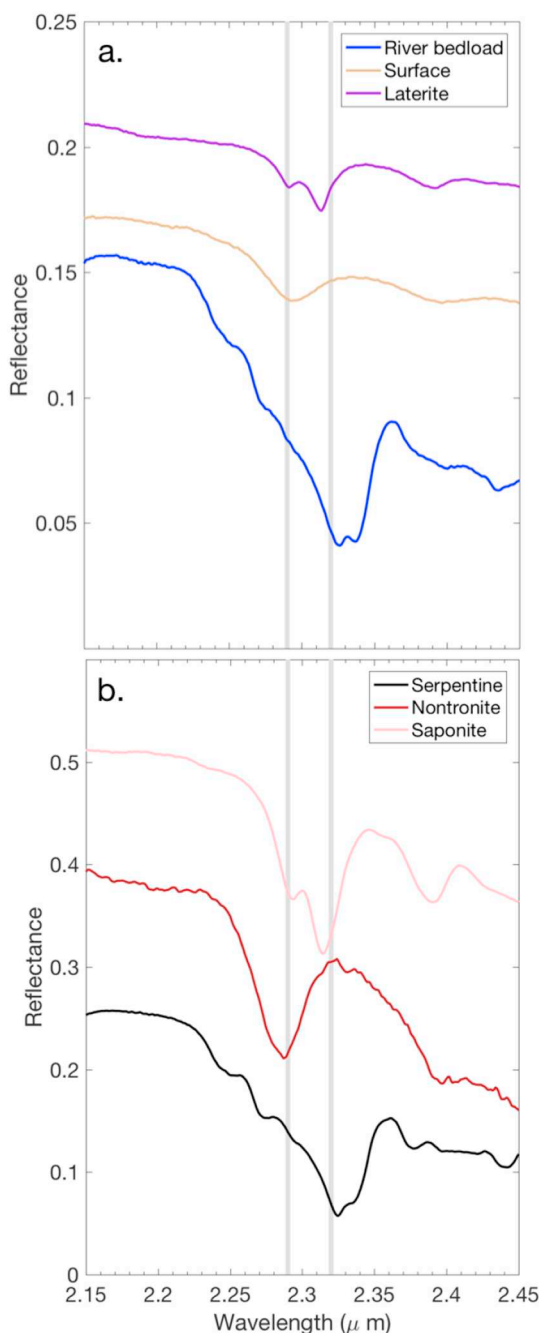


**Fig. 7.** a. Four example reflectance spectra (offset for clarity): a laterite sample, surface sample with 2.28  $\mu\text{m}$  absorptions attributed to nontronite, and Mahalona River bedload sample with no nontronite but a strong 2.32  $\mu\text{m}$  feature attributed to serpentine. b. Laboratory spectra (offset for clarity) of serpentine (lizardite, NMNHR 4687), nontronite (NG-1), and saponite (SapCa-1).

ordering (Fig. 12). Fits to the Mössbauer patterns suggest a significant nanocrystalline component with both  $\text{Fe}^{2+}$  and  $\text{Fe}^{3+}$ . Spectra acquired at the lowest temperature (4 K, Fig. 12) in particular suggest highly disordered, fine-grained material. Only the finest-grained nanophase iron (oxyhydr)oxides would still be unsplit at 4 K, so at least 40% spectral area seems to be attributable to this form of iron (oxyhydr) oxide.

Surface sediment sample 270 (Fig. 12a–c.) is from the northeastern portion of the lake. At 295 K, the Mössbauer fits suggest two unremarkable pairs of ferrous and ferric doublets. One ferrous doublet has a very low IS value and moderate QS value, likely attributable to a clay.

There is no evidence for ilmenite, which should be readily apparent at room temperature. At 130 K, the ferrous phase QS increases only slightly, consistent with the presence of an Fe-bearing clay mineral. A broad sextet appears at this temperature (Fig. 12b., orange curve) that is consistent with magnetite. At 4 K, the ferrous Fe undergoes strong magnetic orientation because of the higher symmetry of the electrons around ferrous Fe. The spectral fits are very complex at this temperature and suggest highly disordered, nanocrystalline phases with both ferrous and ferric components.

Surface sediment sample 286 (Fig. 12d–f.) is from the southern portion of the lake. At 295 K, the parameters are closest to those of ferrous clays or possibly pyroxene (and are inconsistent with olivine, feldspar, sulfate, or phosphate). There is evidence for two ferrous doublets and two ferric doublets at this temperature. At 130 K, the ferric phases move to broad, disordered sextets, consistent with nanophase hematite, goethite, or possibly akaganeite. At 4 K, these sextets are even more prominent and the fits are indicative of significant disorder in the samples. Trace siderite could explain the broad, unsplit blue curve (Fig. 12f.) that disappears at higher temperatures. However, siderite is not apparent in these samples based on VNIR spectra or XRD patterns. If it is present, it is likely  $\leq 5\%$  in abundance, below the approximate detection limit for those methods but possibly still detectable in the Mössbauer data.

## 5. Discussion

The dominant chemical variations observed in Lake Towuti laterites and surface sediments are in Mg, Al, and Fe content. In the lake, Mg and Al abundances are strongly linked to detrital mineralogy, particularly the relative abundance of detrital Mg-serpentine versus kaolinite from the catchment (Fig. 4, Table 4). The coarser-grained surface samples acquired closer to the Mahalona River are mainly composed of serpentine, which is inherently coarser-grained in this system because the river is transporting fragments of serpentinized peridotite bedrock that have undergone limited chemical alteration from the sediment source region. The abundance of Mg is thus a proxy for serpentine content which is in turn a proxy for grain size because serpentine is the dominant phase in the coarser-grained sediment. This can be seen in the spatial distribution of high-Mg lake surface samples that conforms to the boundaries of the Mahalona delta (Fig. 4b). In contrast, kaolinite (and thus Al) abundance increases in the finer-grained detrital component because it is forming in the soil weathering horizons. To the extent that these relationships hold true through geologic time, lateral and vertical variations in the relative abundance of serpentine and kaolinite may thus record important information about sediment flux, water depth/distance to shoreline, and surface weathering conditions through time. The ability of VNIR reflectance spectroscopy to accurately identify and distinguish kaolinite from serpentine, both of which are 7 Å clay minerals, highlights the usefulness of this technique for rapid, non-destructive analysis of sediments and sediment cores to help infer paleoenvironmental conditions in the Malili Lakes system.

Variations in the Fe mineralogy from source to sink reflect complex and dynamic cycling of Fe between a range of mineral hosts that vary in crystallinity and grain size. Elemental Fe abundances are very high in the catchment soils, which represent a major sediment source region, and are consistent with intense weathering in tropical laterites. XRD and spectral analyses of the catchment soils show that they are characterized by a range of crystalline Fe oxides, with goethite being the dominant phase accompanied by lesser amounts of hematite, likely derived from weathering of primary Fe-bearing minerals (e.g., olivine and pyroxene). Magnetite is also present in several samples and appears to be more abundant at greater soil depths, consistent with at least some of the magnetite originating from unweathered bedrock, as suggested in Morlock et al. (2018). Magnetite is also removed and/or segregated during weathering, consistent with its almost complete absence in river samples and deep-water surface samples. Indeed, XRD analyses show



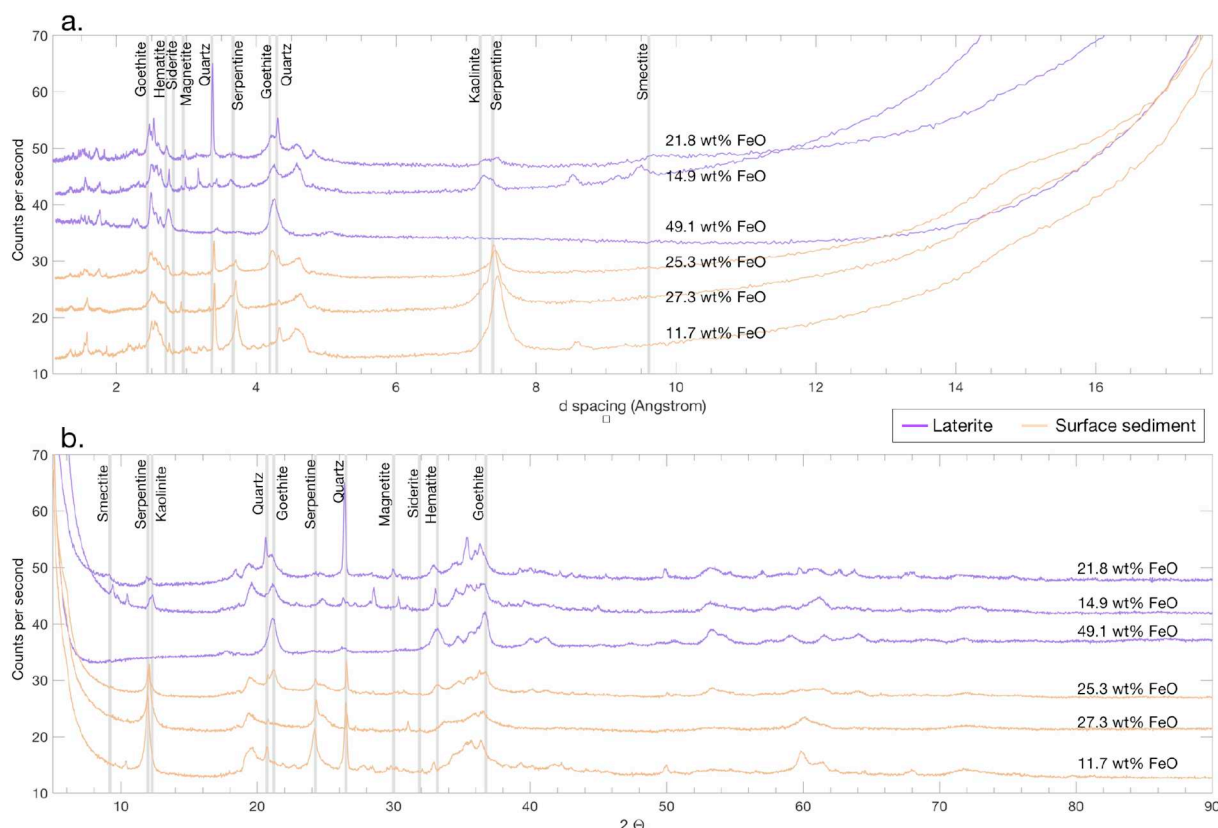


**Fig. 8.** XRD patterns (offset for clarity) of three laterites (purple) and three surface samples (tan) presented in terms of *a.* d-spacing and *b.*  $2\theta$ . Patterns are offset for clarity and labeled with the samples' ICP-determined FeO abundance (wt%). Vertical gray bars highlight the peak location of relevant phases. (For interpretation of the references to colour in this figure legend, the reader is referred to the web version of this article.)

that hematite and magnetite are only present in a few of the shallow coastal samples and these phases are largely absent from deep water samples and from the Mahalona River delta. This is consistent with several processes, including early hydrodynamic settling of magnetite in shallow water due to its higher density (Tamuntuan et al., 2015), reductive dissolution of hematite and magnetite in anoxic water, and variations in sediment source regions, particularly lithologies low in iron in the Mahalona catchment.

The broadening and decrease in peak height seen in XRD patterns of the lake surface samples (Figs. 8, 9) can be explained by a combination of reduction of Fe oxide abundance, decreased grain size, and disorder in the crystal lattice (Sklute et al., 2018). The majority of VNIR spectra for the lake surface samples do exhibit absorptions consistent with the presence of  $\text{Fe}^{2+}/3+$ , in agreement with the measured high  $\text{Fe}_{\text{total}}$  concentrations, but the shapes and positions of these features are not consistent with the presence of only well-crystalline goethite and/or hematite. The dominance of poorly crystalline Fe oxides in the lake surface sediments is also confirmed by Mössbauer measurements, which are consistent with a significant fraction of the Fe in the lake sediments being in the form of nanocrystalline Fe oxides.

Within the lake itself, dissolved oxygen declines below 100 m depth and reaches anoxic conditions around 130 m depth, consistent with evidence that the water-sediment interface is oxic at shallow sites and anoxic and enriched in ferrous Fe at intermediate and deep sites (Vuillemin et al., 2016). Despite the decline (and in some cases absence) of XRD peaks associated with crystalline Fe-oxides and the dominance of such phases in the laterite source regions, ICP results show that many lake surface samples contain high concentrations of  $\text{Fe}_{\text{total}}$ . The total Fe content in surface sediment and down-core samples are similar, but surface samples are roughly equal in their distribution of crystalline and amorphous Fe (based on Fe in the supernatant after

each extraction step), whereas all core samples have more Fe in amorphous phases and a lesser amount in well-crystalline Fe-oxides such as goethite. Interestingly, goethite is present across the lake at the sediment/water interface, although greatly reduced in abundance compared with the catchment soils. The loss of goethite is likely due to its reduction in the anoxic water column and under anoxic conditions at shallow depths beneath the sediment-water interface. However, some goethite persists in the lake samples from the sediment/water interface, even those obtained from deep parts of the lake below anoxic waters. This, together with the persistence of goethite after sequential Fe extractions, suggest that some portion of the goethite may be more resistant to alteration/diagenesis. The cause of this is unknown but may result from goethite acting as a cementing agent, thus forming slightly larger particles that may be more resistant to dissolution. Although some goethite remains in the surface sediment of Lake Towuti, it is likely to be removed over time during burial and early diagenesis. Regardless of the persistence of some goethite, a key observation is that a significant fraction of Fe in the lake surface sediment cannot be accounted for by the crystalline Fe-oxides that are observed in XRD patterns, despite the fact that the majority of Fe likely enters the lake in this form. This suggests that much of the Fe within the lake may be in the form of poorly crystalline, X-ray amorphous phases that originate from the transformation of soil-derived Fe oxides by iron cycling and reduction within the lake.

The changes in Fe mineralogy between sediment source (laterite) and sink (sedimentation in the lake) must account for the increase in amorphous Fe material. If laterites accurately represent a primary sediment input into the lake (aside from the Mahalona delta region), some process or suite of processes acts to liberate iron from the ferric crystalline phases in the water column or shortly after deposition and promotes the formation of new nanocrystalline Fe-oxide phases.



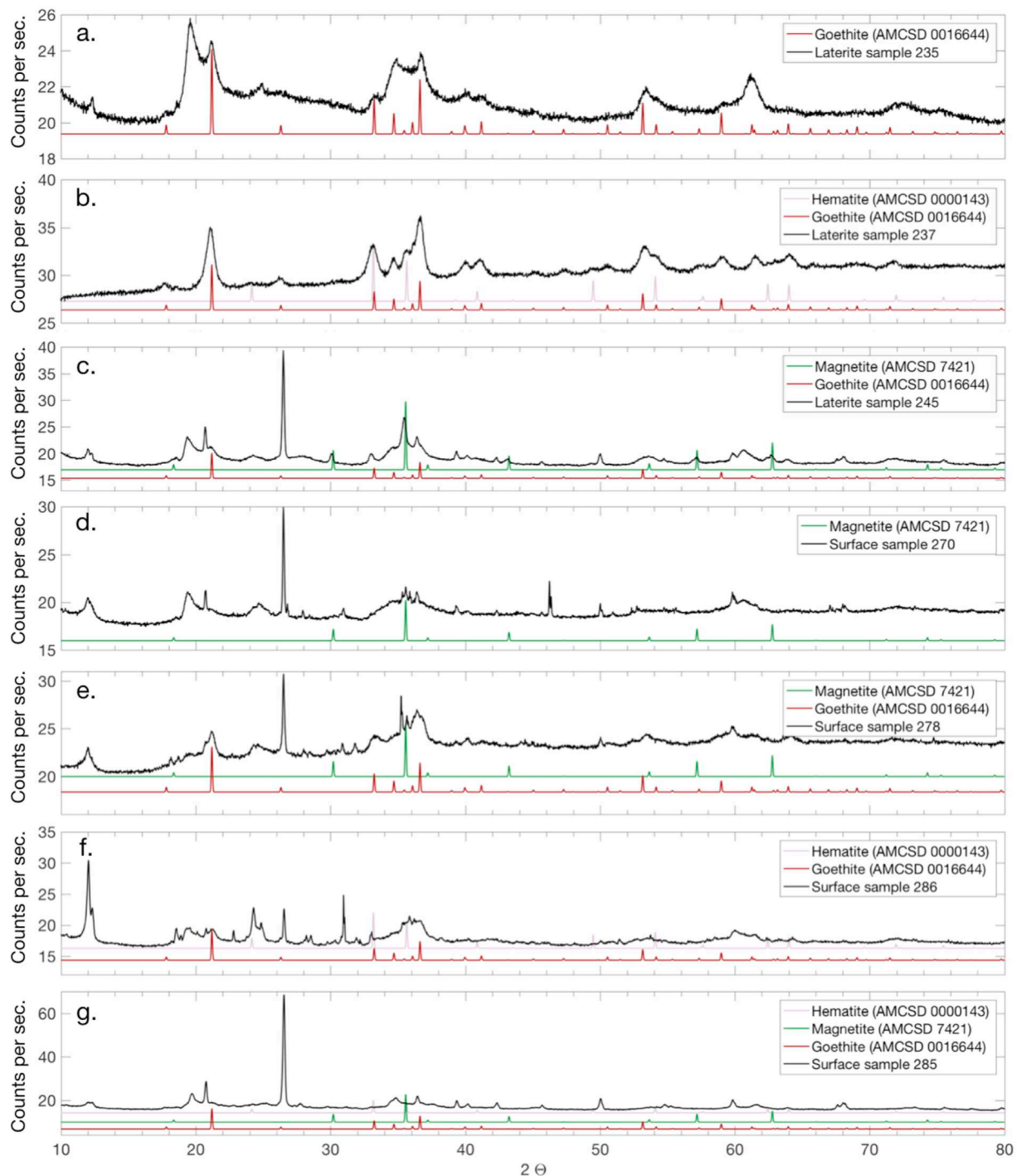


**Fig. 9.** XRD patterns (offset for clarity) from (a–c.) laterites and (d–g.) surface sediment. *a.* A laterite with abundant goethite. *b.* A laterite with abundant goethite and hematite. *c.* A laterite with magnetite and a small amount of goethite. *d.* A surface sample with magnetite. *e.* A surface sample with magnetite and goethite. *f.* A surface sample with goethite and hematite. *g.* A surface sample with no discernible Fe oxides present. Note that the common sharp peak at 26.4° 2θ is quartz.

Interestingly, and despite Lake Towuti being redox-stratified, there is no clear correlation between the relative abundance of crystalline Fe oxides in the surface sediments and water depth: most surface sediments that were sampled at water depths above the modern oxycline also exhibit less goethite and hematite than observed in soils even though total Fe content remains high. This, together with the presence of goethite in sediments below the oxycline indicates there is less of a gradient in Fe mineralogy across the modern oxycline than might be expected if water column reduction reactions control the Fe mineralogy in the lake. Possible explanations for the apparent relative

“homogeneity” in Fe oxide mineralogy at different water depths include: (i) conditions, perhaps biologically mediated, in shallow water settings allow for some reductive dissolution of Fe, presumably along redox gradients at shallow depth in the sediment, or (ii) reduction of Fe oxides in deep water followed by frequent water column mixing to precipitate more oxidized species across the lake.

Fe cycling has been studied in the water column of Lake Matano, another of the Malili lakes that is non-sulfidic, permanently redox-stratified, and more than twice as deep as Lake Towuti (Crowe et al., 2011). Studies of its water column chemistry have shown that the

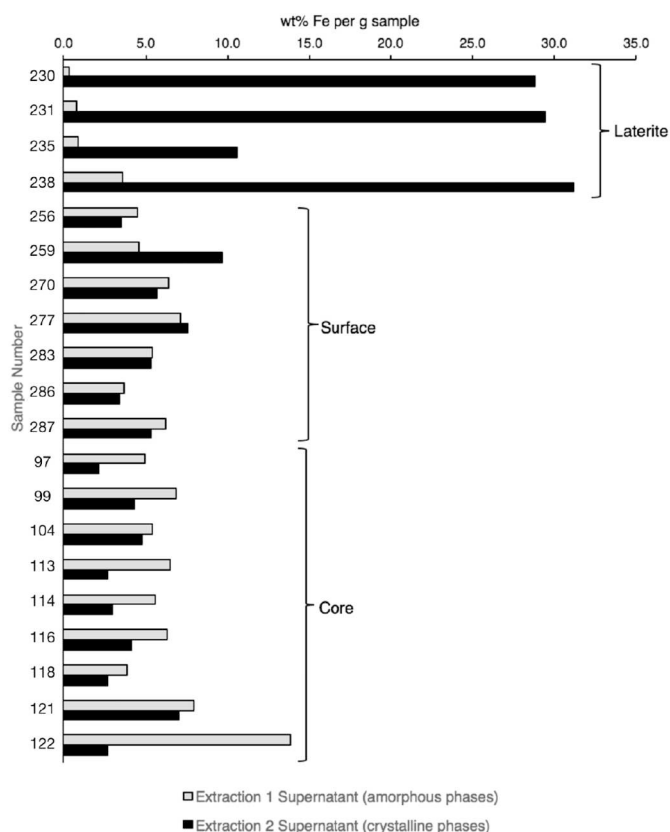


**Fig. 10.** Comparison of the wt% Fe per g sample in each supernatant produced via extraction 1 (gray, amorphous phases) and extraction 2 (black, crystalline phases). Laterite samples are from depths of 10 cm to 2 m from the surface; core samples are from 2 to 77 m sediment depth, with one tephra (sample 20); surface samples represent sediment depths of < 5 cm and are from varying locations, including one from the Mahalona delta (sample 5). Differences in the level of noise between patterns is due to differences in integration times. Values of 2 were adjusted slightly to account for minor sample displacement, normalizing such that the primary quartz peak is centered at 26.6 degrees 2. Sample numbers are that of the original sediment; see Table 1 for more information.

surface mixed layer of Lake Matano is in a pH/pE range in which iron (hydr)oxides are stable, whereas the hypolimnion favors  $\text{Fe}(\text{OH})^{2+}$  and  $\text{Fe}^{2+}$  (Crowe et al., 2008). It is possible that similar cycling promotes the transformation of the crystalline Fe oxide form to more nanophase components. Ferric oxides may settle below the oxycline where they are then rapidly reduced and/or altered to amorphous phases. Though we cannot exclude authigenic formation of goethite, based on the results presented here it seems more likely that some of the incoming goethite is relatively resistant and is slow to undergo reductive dissolution. The lake is very S-poor, thus appreciable quantities of pyrite do not form even below the oxycline. Fe that is reduced and dissolved at depth, either in the water column or in the sediment, can migrate upward to form new amorphous Fe phases in the water column or in very shallow sediment. Occasional lake mixing events may form substantial quantities of new  $\text{Fe}^{3+}$ -bearing minerals that are spread throughout the lake. This would be consistent with the conclusions of Tamuntuan et al. (2015) that the main factor driving diagenesis within short sediment cores is iron oxide dissolution.

### 5.1. Lake Towuti as an analogue for martian paleolakes?

The mafic/ultramafic East Sulawesi Ophiolite shares some compositional similarities with the mafic martian crust (Bibring et al., 2005;

McSween et al., 2009; Kadarusman et al., 2004). Examining chemical and mineralogical relationships in Mg/Fe-rich sediment in the Lake Towuti system may have implications for interpreting geochemical data of ancient lacustrine mudstones on Mars (Weber et al., 2015; Goudge et al., 2017).

The NASA Mars Curiosity rover is currently characterizing the chemistry and mineralogy of a ~5 km thick sequence of strata informally known as Mt. Sharp that is hosted within Gale Crater (Grotzinger et al., 2014). The overall abundance of FeO has remained relatively constant for a large part of the stratigraphic section; however, the mineral hosts of Fe have changed tremendously (e.g. Hurowitz et al. (2017); Rampe et al. (2017)), leading to various theories on the structure of the lake, as discussed more below. In Lake Towuti, there is a similar overall steadiness in elemental  $\text{Fe}_{\text{total}}$  (Figs. 5, 10) with great diversity in Fe mineralogy (Fig. 8). While redox transformations of iron do support many types of microbial life, especially in warm tropical environments, this will catalyze reactions that may otherwise be thermodynamically feasible without them, increasing the rate but not necessarily fundamentally altering the way iron may be cycled in the environment (Davison, 1993). Though the tropical setting of the Towuti system is not a perfect analogue for Mars, and though biology and the presence of organic matter undoubtedly play an important role in redox reactions, it nevertheless provides a modern setting for understanding how to infer sediment-water interactions in a redox stratified lake via chemical and mineralogical information. In the case of Lake Towuti, VNIR reflectance spectra are linked to chemical and mineralogical trends in bulk sediment samples. Similarly, certain elements (Al, Mg) provide useful proxies for mineralogy. Combined with bulk chemical measurements, VNIR spectra thus provide a rapid and non-destructive means to gain a first order understanding of sediment deposition and diagenesis across modern Lake Towuti and presumably through time, and similar approaches may be applied to lacustrine sequences on Mars.

The mudstones of Mt. Sharp in particular contain a range of hydrous and Fe-bearing minerals, including primary igneous phases (olivine, pyroxene), sulfides/sulfates, Fe-bearing clay minerals, hematite, and magnetite (Grotzinger et al., 2014; Vaniman et al., 2014; Rampe et al., 2017). Trends in the chemistry and mineralogy of these rocks are still being examined, but variations in Fe mineralogy and oxidation state have been observed as a function of stratigraphic position by the rover (Hurowitz et al., 2017) as well as from orbit (Milliken et al., 2010). Variations in iron mineralogy, and correlations between elements such as Zn, Ni, and Si, have been interpreted as evidence for changing martian environmental conditions during the evolution of the Gale crater lake. Hurowitz et al. (2017) recently suggested that some observations are consistent with the presence of a redox-stratified lake in which oxidizable cations become enriched through photo-oxidation of reduced (ferrous) groundwaters that seep into the lake. In this model, mineral assemblages vary as a function of lake water depth, wherein magnetite and silica phases precipitate in the reducing deep water below the oxycline and hematite-phylosilicate assemblages reflect more oxidizing, shallow water influenced by the surface environment. The transition from magnetite and clay-bearing facies to strata dominated by hematite and sulfate, in addition to recent identification of potential desiccation cracks in the mudstones, may be evidence of fluctuations in lake level. However, others have suggested that trends in redox-sensitive elements in Gale Crater indicate acid sulfate alteration of mafic materials (Yen et al., 2017; Rampe et al., 2017).

Characterizing the chemistry and mineralogy of sediments in a modern terrestrial redox stratified lake in a mafic/ultramafic catchment can also provide useful information on sediment transport and alteration processes, as well as evidence of what environmental factors may ultimately be recorded in the sedimentary rock record. In the Malili Lakes system, VNIR spectral characteristics can be used to infer both chemistry and mineralogy (Weber et al., 2015; Goudge et al., 2017), and this has relevant applications for the study of martian paleolake basins. Strata in Gale Crater, for example, has orbital spectral evidence

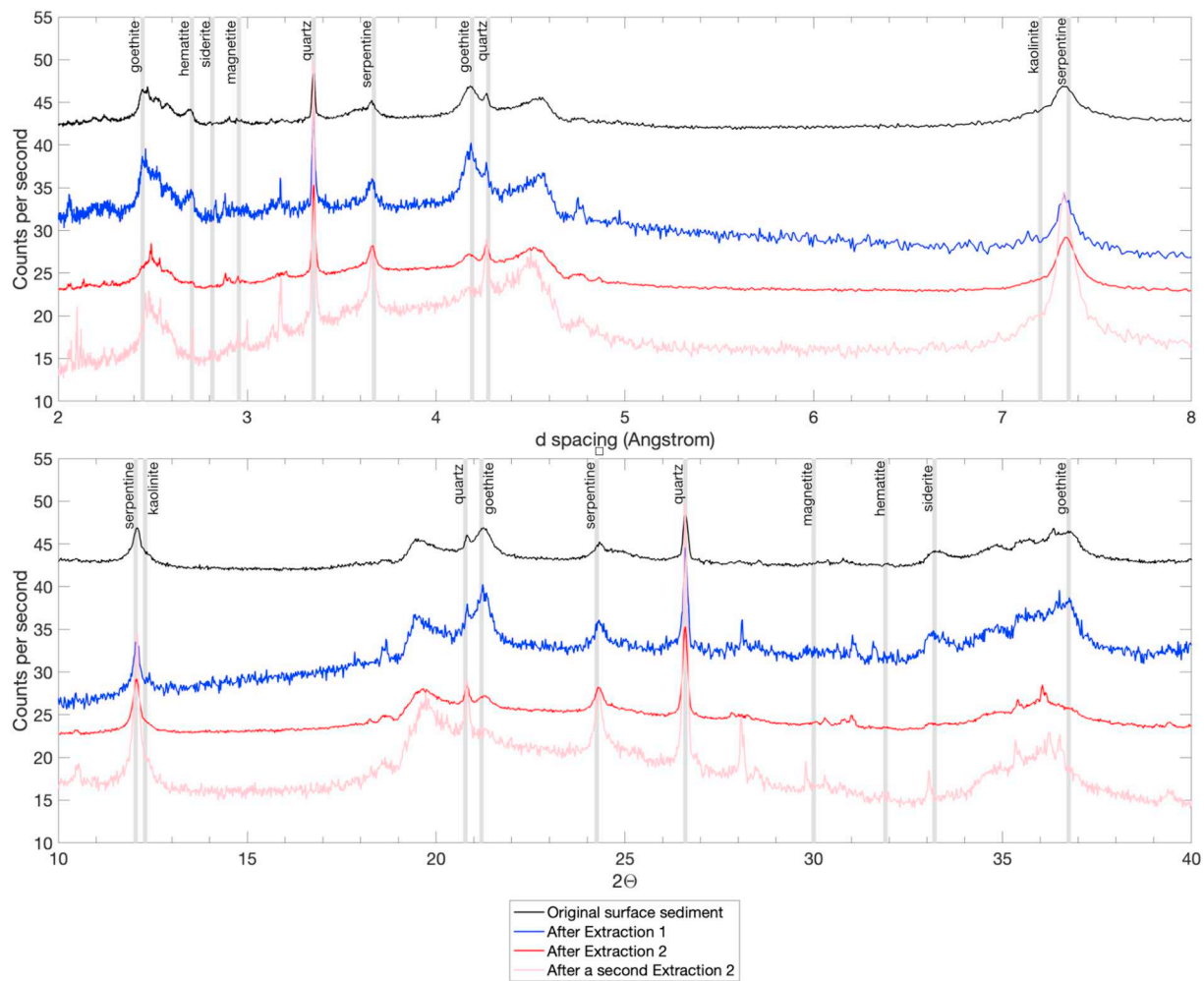


**Fig. 11.** Zoomed-in XRD patterns (offset for clarity) of one surface sample (sample 259) throughout the sequential extraction process in terms of *a.* d-spacing and *b.*  $2\theta$ . Patterns are offset for clarity and diagnostic peaks of relevant phases are highlighted in gray.

of clay minerals (Milliken et al., 2010), in situ XRD measurements that confirm the presence of clays in this crater, and evidence for significant fractions of X-ray amorphous components (Grotzinger et al., 2014; Vaniman et al., 2014; Rampe et al., 2017). Rover payloads are inherently limited in terms of analytical ability, and understanding source regions and hydrologic history through clay mineralogy in martian paleolakes requires distinguishing chemical and mineralogical trends using remote techniques such as VNIR spectroscopy (Ehlmann et al., 2008; Milliken et al., 2010). Lake Towuti is a useful analogue in that it provides proof of the link between chemistry, mineralogy, and spectroscopy in lacustrine sediments.

One intriguing observation in Lake Towuti sediments that may be useful for understanding martian counterparts is the relationship between the abundance of Si and Ti. A positive correlation between these elements has been observed at several sites on Mars, including lacustrine mudstones in Gale Crater and non-lacustrine rocks and soils in Gusev Crater. This trend has been cited as evidence for acid sulfate leaching in both locations (Squyres et al., 2008; Morris et al., 2008; Yen et al., 2017; Rampe et al., 2017). A similar correlation is seen in Lake Towuti sediment samples (positive coefficient significant at  $p < 0.01$ ) (Fig. 13, Table 6), where it has been interpreted to be driven by trends in physical weathering and transport under different climate conditions (i.e. the integration of rainfall, erosion, and fluvial discharge in the area). An increase in Ti concentration in this system has been used as a proxy for increased physical weathering and runoff in the source region because this leads to an increase in the detrital influx of rutile and/or

ilmenite (Russell et al., 2014). The similarity of the strong positive correlation between Si and Ti in the circum-neutral (Costa et al., 2015) Lake Towuti system suggests that lacustrine sediments in Gale Crater that exhibit this elemental relationship need not have been formed in or affected by low-pH fluids, particularly if Ti-bearing phases are available and variable in the sediment source region.

As with any terrestrial analogue, the influence of organic matter and biology on the rate of redox processes in Towuti must be considered, though Lake Towuti is notable for being one of the least productive tropical lakes on the planet (Haffner et al., 2001). Nontronite is also a useful mineral for addressing the water oxidation state on Earth and Mars. There is evidence that this ferric smectite may form from ferrous precursors precipitated under initially reducing conditions (Muller and Forstner, 1973; Harder, 1976; Pedro et al., 1978; Decarreau and Bonnin, 1986), and thus its presence could indicate a change in oxidation state. Nontronite has been identified in several places on Mars, including Gale Crater (Poulet et al., 2005; Bishop et al., 2008; Milliken et al., 2010; Ehlmann et al., 2009), and it seems to be present in some of the Towuti laterite samples and thus may represent a detrital component in the lake surface samples. However, if some of the nontronite in the lake sediments is authigenic then it could provide valuable information on changes in the redox interface in Lake Towuti at those locations, and future study of this phase in these samples is warranted. Similarly, in situ identification of nontronite by Curiosity could be used to constrain redox conditions and evolution in the Gale crater lake, particularly if it over or underlies beds with greater proportions of ferric oxides.

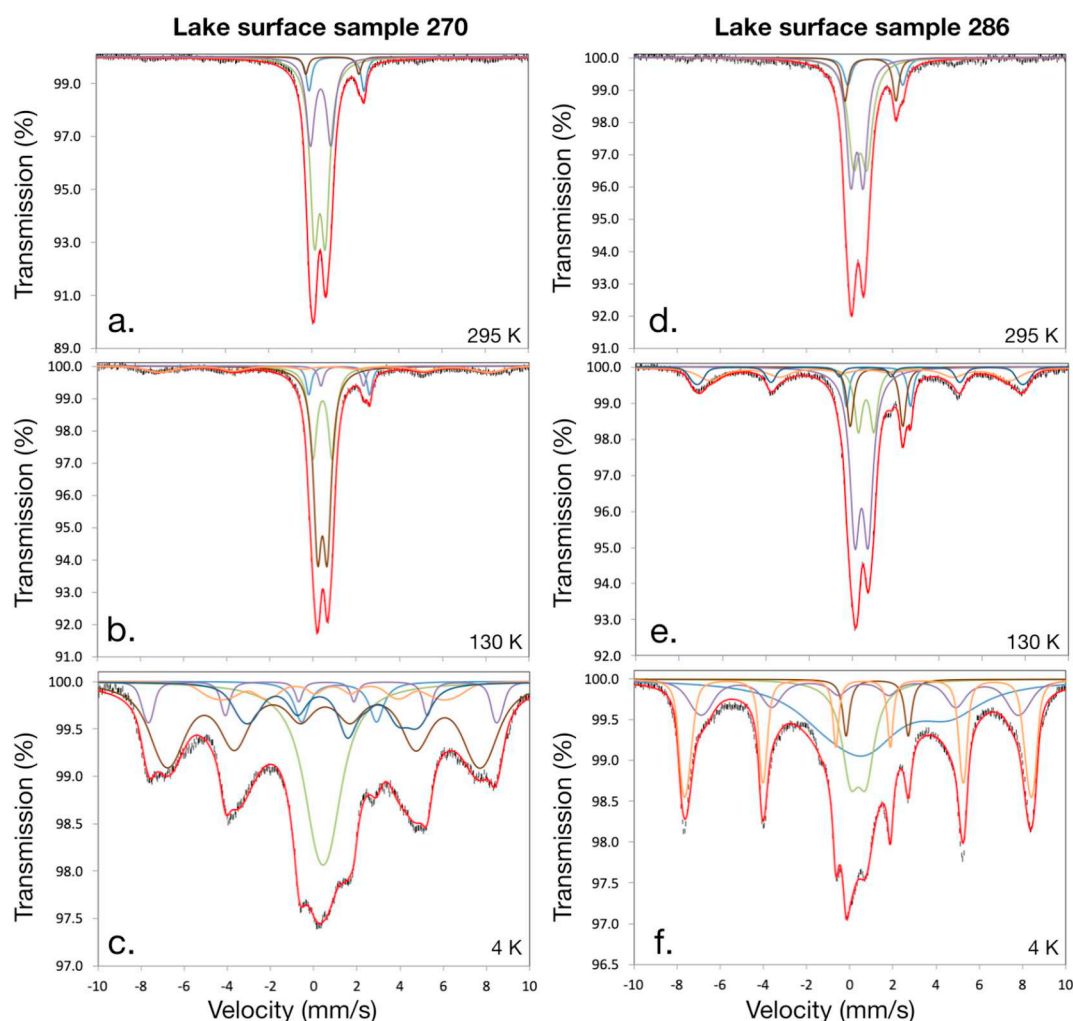


**Fig. 12.** Mössbauer spectra (black line) and fits (colored lines) for surface sample 270 at a. 295 K, b. 130 K, and c. 4 K. Mössbauer spectra (black line) and fits (colored lines) for surface sample 286 at d. 295 K, e. 130 K, and e. 4 K.

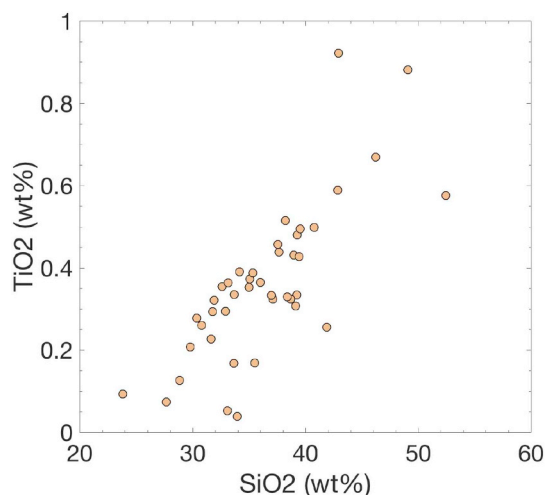


**Fig. 13.** ICP-determined Si and Ti abundances for Lake Towuti surface samples.

## 6. Conclusions

Sediment throughout the Malili Lakes system is highly variable in terms of mineralogy and bulk chemistry, particularly with respect to the type and abundance of secondary Fe-bearing phases. VNIR spectral

**Table 6**  
Si Ti regression results.

	Dependent variable
	TiO <sub>2</sub> , surface
SiO <sub>2</sub> , surface	0.026*** (0.003)
Constant	−0.594*** (0.125)
Observations	42
R <sup>2</sup>	0.597
Residual Std. error	0.121 (df = 40)
F statistic	59.187*** (df = 1; 40)

Note: \* $p < 0.1$ ; \*\* $p < 0.05$ ; \*\*\* $p < 0.01$ .

parameters are well correlated with the relevant ICP elemental abundances, demonstrating that reflectance spectra, which require little to no sample preparation, can provide a useful, rapid way to infer bulk chemistry of these sediments. The role and distribution of Fe in Lake Towuti is complex: abundant, easily characterizable crystalline Fe phases in lateritic soils are rapidly altered after deposition on the lake surface to complex forms of Fe, as seen in XRD patterns, VNIR reflectance spectra, and Mössbauer spectra. The processes that drive observed changes in Fe mineralogy are not known with certainty, but Towuti is a redox-stratified lake with low primary productivity, thus the observed changes could be facilitated by Fe cycling across the oxycline.



Consistent with this, sequential Fe extractions show a decrease in the ratio of crystalline to amorphous Fe phases through the transport system from laterites to surface sediment to cores. The spatial variability in Fe hosts across the modern lake sediment surface is likely affected by variations in source composition as well as Fe cycling in the water column and early diagenetic processes. Understanding the effects of transport, deposition, and diagenesis on sediment composition, particularly changes in Fe mineralogy, in a terrestrial mafic/ultramafic system such as Lake Towuti will continue to aid in the interpretation and climatic reconstruction of this region, and these results may also have utility for interpreting Fe-rich mineral assemblages in lacustrine sediments observed on Mars.

## Acknowledgments

Funding for laboratory experiments was provided by Brown University Presidential Fellowship. Sample collection during the Towuti Drilling Project was supported by grants from the International Continental Scientific Drilling Program (ICDP, grant #2013-02), the US National Science Foundation (NSF-EAR #1401448), the German Research Foundation (DFG; ME 1169/26), the Swiss National Science Foundation (SNSF; 20FI21\_153054/1 & 200021\_153053/1&2), Brown University, Genome British Columbia, and the Ministry of Research, Technology, and Higher Education (RISTEK). PT Vale Indonesia and the US Continental Drilling Coordination Office are acknowledged for the logistical assistance to the project. This research was carried out with permission from RISTEK, the Ministry of Trade of the Government of Indonesia, the Natural Resources Conservation Center (BKSDA), and the Government of Luwu Timur of Sulawesi. Mössbauer analyses were funded by Brown University SSERVI. We are very grateful to Dave Murray and Joe Orchard for assistance with the ICP-AES and to Luis Gabriel Ordonez Rendon for advice on the sequential extraction protocol. Christopher Yen and Grant Rutherford assisted in laboratory work and data collection. Sample material was provided in part by the National Lacustrine Core Facility (LacCore).

## References

- Bibring, J.-P., Langevin, Y., Gendrin, A., Gondet, B., Poulet, F., Berthe, M., Soufflot, A., Arvidson, R., Mangold, N., Mustard, J., Drossart, P., 2005. The OMEGA team: Mars surface diversity as revealed by the OMEGA/Mars Express observations. *Science* 307, 1576–1581.
- Bishop, J.L., Lane, M.D., Dyar, M.D., Brown, A.J., 2008. Reflectance and emission spectroscopy study of four groups of phyllosilicates: smectites, kaolinite-serpentines, chlorites and micas. *Clay Miner.* 43 (1), 35–54.
- Burns, R.G., 1993. *Mineralogical applications of crystal field theory*. Cambridge University Press.
- Clark, R.N., Roush, T.L., 1984. Reflectance spectroscopy: quantitative analysis techniques for remote sensing applications. *JGR* 89 (7), 6329–6340.
- Clark, R.N., King, T.V.V., Klejwa, M., Swayze, G.A., Vergo, N., 1990. High spectral resolution reflectance spectroscopy of minerals. *J. Geophys. Res.* 95 (B8), 12653–12680.
- Costa, K.M., Russell, J.M., Vogel, H., Bijaksana, S., 2015. Hydrological connectivity and mixing of lake towuti, Indonesia in response to paleoclimatic changes over the last 60,000 years. *Palaeogeogr. Palaeoclimatol. Palaeoecol.* 417, 467–475.
- Crowe, S.A., O'Neill, A.H., Katsev, S., Hehanussa, P., Haffner, G.D., Sundby, B., Mucci, A., Fowle, D.A., 2008. The biogeochemistry of tropical lakes: a case study from Lake Matano, Indonesia. *Limnol. Oceanogr.* 53 (1), 319–331.
- Crowe, S.A., Katsev, S., Leslie, K., Sturm, A., Magen, C., Nomosatryo, S., Pack, M.A., Kessler, J.D., Reeburgh, W.S., Roberts, J.A., Gonzalez, L., Douglas Haffner, G., Mucci, A., Sundby, B., Fowle, D.A., 2011. The methane cycle in ferruginous Lake Matano. *Geobiology*. <https://doi.org/10.1111/j.1472-4669.2010.00257.x>.
- Davison, W., 1993. Iron and manganese in lakes. *Earth Sci. Rev.* 34 (2), 119–163. [https://doi.org/10.1016/0012-8252\(93\)90029-7](https://doi.org/10.1016/0012-8252(93)90029-7) ISSN 0012-8252.
- Decarreau, A., Bonnin, D., 1986. Synthesis and crystallogeneses at low temperature of Fe (III)-smectites by evolution of coprecipitated gels: experiments in partially reducing conditions. *Clay Miner.* 21, 861–877.
- Dyar, M., Darby, Agresti, David G., Schaefer, Martha W., Grant, Christopher A., Sklute, Elizabeth C., 2006. Mössbauer spectroscopy of earth and planetary materials. *Annu. Rev. Earth Planet. Sci.* 34, 83–125.
- Ehlmann, B.L., Mustard, J.F., Fassett, C.I., Schon, S.C., Head III, J.W., Des Marais, D.J., Grant, J.A., Murchie, S.L., 2008. Clay minerals in delta deposits and organic preservation potential on Mars. *Nat. Geosci.* 1, 355–358.
- Ehlmann, B.L., Mustard, J.F., Swayze, G.A., Clark, R.N., Bishop, J.L., Poulet, F., Marais, D.J.D., Roach, L.H., Milliken, R.E., Wray, J.J., Barnouin-Jha, O., Murchie, S.L., 2009. Identification of hydrated silicate minerals on Mars using MRO-CRISM: geologic context near Nili Fossae and implications for aqueous alteration. *J. Geophys. Res. Planets* 114.
- Gaffey, S.J., McFadden, L.A., Nash, D., Pieters, C.M., 1993. Remote geochemical analysis: elemental and mineralogical composition. In: *Chapter Ultraviolet, Visible, and Near-Infrared Reflectance Spectroscopy: Laboratory Spectra of Geologic Materials*. Cambridge University Press, pp. 43–78.
- Goudge, T.A., Russell, J.M., Mustard, J.F., Head, J.W., Bijaksana, S., 2017. A 40,000 yr record of clay mineralogy at Lake Towuti, Indonesia: Paleoclimate reconstruction from reflectance spectroscopy and perspectives on paleolakes on Mars. *GSA Bull.* 129 (7/8), 806–819.
- Grotzinger, J.P., Sumner, D.Y., Kah, L.C., Stack, K., Gupta, S., Edgar, L., Rubin, D., Lewis, K., Schieber, J., Mangold, N., Milliken, R., Conrad, P.G., DesMarais, D., Farmer, J., Siebach, K., Calef III, F., Hurowitz, J., McLennan, S.M., Ming, D., Vaniman, D., Crisp, J., Vasavada, A., Edgett, K.S., Malin, M., Blake, D., Gellert, R., Mahaffy, P., Wiens, R.C., Maurice, S., Grant, J.A., Wilson, S., Anderson, R.C., Beegle, L., Arvidson, R., Hallet, B., Sletten, R.S., Rice, M., Bell III, J., Griffes, J., Ehlmann, B., Anderson, R.B., Bristow, T.F., Dietrich, W.E., Dromart, G., Eigenbrode, J., Fraeman, A., Hardgrove, C., Herkenhoff, K., Jandura, L., Kocurek, G., Lee, S., Leshin, L.A., Leveille, R., Limonadi, D., Maki, J., McCloskey, S., Meyer, M., Minitti, M., Newsom, H., Oehler, D., Okon, A., Palucis, M., Parker, T., Rowland, S., Schmidt, M., Squyres, S., Steele, A., Stolper, E., Summons, R., Treiman, A., Williams, R., Yingst, A., 2014. A habitable fluvio-lacustrine environment at Yellowknife Bay, Gale Crater, Mars. *Science* 343.
- Haffner, G.D., Hehanussa, P.E., Hartoto, D., 2001. The biology and physical processes of large lakes of Indonesia: Lakes Matano and Towuti. In: Munawar, M., Hecky, R.E. (Eds.), *The Great Lakes of the World (GLOW): Food-web, Health and Integrity*. Blackhuys Publishers, pp. 129–155.
- Harder, H., 1976. Nontronite synthesis at low temperatures. *Chem. Geol.* 18, 169–180.
- Hasberg, A.K.M., Bijaksana, S., Held, P., Just, J., Melles, M., Morlock, M.A., Opitz, S., Russell, J.M., Vogel, H., Wennrich, V., 2018. Modern sedimentation processes in Lake Towuti, Indonesia, revealed by the composition of surface sediments. *Sedimentology* 66, 675–698.
- Hurowitz, J.A., Grotzinger, J.P., Fischer, W.W., McLennan, S.M., Milliken, R.E., Stein, N., Vasavada, A.R., Blake, D.F., Dehouck, E., Eigenbrode, J.L., Fairén, A.G., Frydenvang, J., Gellert, R., Grant, J.A., Gupta, S., Herkenhoff, K.E., Ming, D.W., Rampe, E.B., Schmidt, M.E., Siebach, K., Stack-Morgan, K., Sumner, D.Y., Wiens, R.C., 2017. Redox stratification of an ancient lake in Gale Crater, Mars. *Science* 356 (eaah6849).
- Kadarusman, A., Miyashita, S., Maruyama, S., Parkinson, C.D., Ishikawa, A., 2004. Petrology, geochemistry and paleogeographic reconstruction of the East Sulawesi Ophiolite, Indonesia. *Tectonophysics* 392 (1), 55–83.
- McSween, H.Y., Taylor, G.J., Wyatt, M.B., 2009. Elemental composition of the Martian crust. *Science* 324 (5928), 736–739.
- Milliken, R.E., Grotzinger, J.P., Thompson, B.J., 2010. Paleoclimate of Mars as captured by the stratigraphic record in Gale Crater. *Geophys. Res. Lett.* 37. <https://doi.org/10.1029/2009GL041870>.
- Morlock, M.A., Vogel, H., Nigg, V., Ordonez, L., Hasberg, A.K.M., Melles, M., Russell, J.M., Bijaksana, S., 2018. Climatic and tectonic controls on source-to-sink processes through space and time in the tropical ultramafic Lake catchment of Lake Towuti, Indonesia. *J. Paleolimnol.* <https://doi.org/10.1007/s10933-018-0059-3>.
- R. V. Morris, G. Klingelhofer, C. Schroder, I. Fleischer, D. W. Ming, A. S. Yen, R. Gellert, R. E. Arvidson, D. S. Rodionov, L. S. Crumpler, B. C. Clark, B. A. Cohen, T. J. McCoy, D. W. Mittlefehldt, M. E. Schmidt, P. A. de Souza Jr., and S. W. Squyres. Iron Mineralogy and Aqueous Alteration From Husband Hill through Home Plate at Gusev Crater, Mars: Results From the Mössbauer Instrument on the Spirit Mars Exploration Rover. *JGR*, 2008.
- Muller, G., Forstner, U., 1973. Recent iron ore formation in Lake Malawi, Africa. *Mineral. Deposita* 8, 278–290.
- Murray, R.W., Miller, D.J., Kryc, K.A., 2000. Analysis of major and trace elements in rocks, sediments, and interstitial waters by inductively coupled plasma-atomic emission spectrometry (ICP-AES). In: *ODP Technical Note*. 1. pp. 1–27.
- Pedro, G., Carmouze, J.P., Velde, B., 1978. Peloidal nontronite formation in recent sediments of Lake Chad. *Chem. Geol.* 23, 139–149.
- F. Poulet, Bibring J.P., Mustard J.F., Gendrin A., Mangold N., Langevin Y., Arvidson R.E., Gondet, Gomez, Berthe M., Erard S., Forni O., Manaud N., Poulleau G., Soufflot A., Combes M., Drossart P., Encrenaz T., Fouchet T., Melchiorri R., Bellucci G., Altieri F., Formisano V., Fonti S., Capaccioni F., Cerroni P., Coradini A., Korabov O., Kottsov V., Ignatiev N., Titov D., Zasova L., Pinet P., Schmitt B., Sotin C., Hauber E., Hoffmann H., Jaumann R., Keller U., Forget F., and the Omega Team. Phyllosilicates on Mars and implications for early martian climate. *Nature*, 2005.
- Poulton, S.W., Canfield, D.E., 2005. Development of a sequential extraction procedure for iron: implications for iron partitioning in continentally derived particulates. *Chem. Geol.* 214, 209–221.
- Rampe, E.B., Ming, D.W., Blake, D.F., Bristow, T.F., Chipera, S.J., Grotzinger, J.P., Morris, R.V., Morrison, S.M., Vaniman, D.T., Yen, A.S., Achilles, C.N., Craig, P.I., Des Marais, D.J., Downs, R.T., Farmer, J.D., Fendrich, K.V., Gellert, R., Hazen, R.M., Kah, L.C., Morookian, J.M., Peretyazhko, T.S., Sarrazin, J., Treiman, A.H., Berger, J.A., Eigenbrode, J., Fairén, A.G., Forni, O., Gupta, S., Hurowitz, J.A., Lanza, N.L., Schmidt, M.E., Siebach, K., Sutter, B., Thompson, L.M., 2017. Mineralogy of an ancient lacustrine mudstone succession from the Murray formation, Gale crater, Mars. *EPSL* 471, 172–185.
- Russell, J.M., Vogel, H., Konecky, B.L., Bijaksana, S., Huang, Y., Melles, M., Wattrus, N., Costa, K., King, J.W., 2014. Glacial forcing of central Indonesian hydroclimate since 60,000 y B.P. *PNAS* 111 (14), 5100–5105.
- Russell, J.M., Bijaksana, S., Vogel, H., Melles, M., Kallmeyer, J., Ariztegui, D., Crowe, S., Fajar, S., Haridz, A., Haffner, D., Hasberg, A., Ivory, S., Kelly, C., King, J., Kirana, K.,

- Morlock, M., Noren, A., O'Grady, R., Ordonez, L., Stevenson, J., von Rintelen, T., Vuillemin, A., Watkinson, I., Wattrus, N., Wicaksono, S., Wonik, T., Bauer, K., Deino, A., Friese, A., Henny, C., Imran, R. Marwoto, Ngkoimani, L.O., Nomosatryo, S., Safiuddin, L.O., Simister, R., Tamuntuan, G., 2016. The Towuti Drilling Project: paleoenvironments, biological evolution, and geomicrobiology of a tropical Pacific lake. *Sci. Drill.* 21, 29–40.
- Sklute, Elizabeth C., Kashyap, Srishti, Dyar, M. Darby, Holden, James F., Tague, Thomas, Wang, Peng, Jaret, Steven J., 2018. Spectral and morphological characteristics of synthetic nanophase iron (oxyhydr)oxides. *Phys. Chem. Miner.* 45 (1).
- Squyres, S.W., Arvidson, R.E., Ruff, S., Gellert, R., Morris, R.V., Ming, D.W., Crumpler, L., Farmer, J.D., Des Marais, D.J., Yen, A., McLennan, S.M., Calvin, W., Bell III, J.F., Clark, B.C., Wang, A., McCoy, T.J., Schmidt, M.E., de Souza Jr., P.A., 2008. Detection of silica-rich deposits on Mars. *Science* 320, 1063–1067.
- Sutter, B., Dalton, J.B., Ewing, S.A., Amundson, R., McKay, C.P., 2007. Terrestrial analogs for interpretation of infrared spectra from the martian surface and subsurface: Sulfate, nitrate, carbonate, and phyllosilicate-bearing Atacama Desert soils. *J. Geophys. Res.* 112 (G04S10).
- Tamuntuan, G., Bijaksana, S., King, J., Russell, J., Fauzi, U., Maryunani, K., Aufa, N., Safiuddin, L.O., 2015. Variation of magnetic properties in sediments from Lake Towuti, Indonesia, and its paleoclimatic significance. *Palaeogeogr. Palaeoclimatol. Palaeoecol.* 420, 163–172.
- Vaniman, D.T., Bish, D.L., Ming, D.W., Bristow, T.F., Morris, R.V., Blake, D.F., Chipera, S.J., Morrison, S.M., Treiman, A.H., Rampe, E.B., Rice, M., Achilles, C.N., Grotzinger, J.P., McLennan, S.M., Williams, J., Bell III, J.F., Newsom, H.E., Downs, R.T., Maurice, S., Sarrazin, P., Yen, A.S., Morookian, J.M., Farmer, J.D., Stack, K., Milliken, R.E., Ehlmann, B.L., Sumner, D.Y., Berger, G., Crisp, J.A., Hurowitz, J.A., Anderson, R., Des Marais, D.J., Stolper, E.M., Edgett, K.S., Gupta, S., Spanovich, N., 2014. Mineralogy of a Mudstone at Yellowknife Bay, Gale Crater. *Mar. Sci.* 343.
- Vogel, H., Russell, J.M., Cahyarini, S.Y., Bijaksana, S., Wattrus, N., Rethemeyer, J., Melles, M., 2015. Depositional modes and lake-level variability at Lake Towuti, Indonesia, during the past 29 kyr BP. *J. Paleolimnol.* <https://doi.org/10.1007/s10933-015-9857-z>.
- Vuillemin, A., Friese, A., Alawi, M., Henny, C., Nomosatryo, S., Wagner, D., Crowe, S.A., Kallmeyer, J., 2016. Geomicrobiological features of ferruginous sediments from Lake Towuti, Indonesia. *Front. Microbiol.* <https://doi.org/10.3389/fmicb.2016.01007>.
- Wagner, C., Schade, U., 1996. Measurements and calculations for estimating the spectrometric detection limit for carbonates in Martian soil. *Icarus* 123 (0156), 256–268.
- Weber, A.K., Russell, J.M., Goudge, T.A., Salvatore, M.R., Mustard, J.F., Bijaksana, S., 2015. Characterizing clay mineralogy in Lake Towuti, Indonesia, with reflectance spectroscopy. *J. Paleolimnol.* 54 (2), 253–261.
- Yen, A.S., Ming, D.W., Vaniman, D.T., Gellert, R., Blake, D.F., Morris, R.V., Morrison, S.M., Bristow, T.F., Chipera, S.J., Edgett, K.S., Treiman, A.H., Clark, B.C., Downs, R.T., Farmer, J.D., Grotzinger, J.P., Rampe, E.B., Schmidt, M.E., Sutter, B., Thompson, L.M., 2017. Multiple stages of aqueous alteration along fractures in mudstone and sandstone strata in Gale Crater, Mars. *Earth Planet. Sci. Lett.* 471, 186–198.